2021

Proteomic and functional mapping of cardiac NaV1.5 channel phosphorylation sites

Maxime Lorenzini

Emily Wagner

Kiersten M. Ruff

Rohit V. Pappu

Jeanne M. Nerbonne

See next page for additional authors

Authors

Maxime Lorenzini, Emily Wagner, Kiersten M. Ruff, Rohit V. Pappu, Jeanne M. Nerbonne, Jonathan R. Silva, R. Reid Townsend, and et al

JGP Journal of General Physiology

ARTICLE

Proteomic and functional mapping of cardiac $Na_V1.5$ channel phosphorylation sites

Maxime Lorenzini[1], Sophie Burel[1], Adrien Lesage[1], Emily Wagner[2], Camille Charrière[1], Pierre-Marie Chevillard[1], Bérangère Evrard[1], Dan Maloney[3], Kiersten M. Ruff[2], Rohit V. Pappu[2], Stefan Wagner[4], Jeanne M. Nerbonne[5,6], Jonathan R. Silva[2], R. Reid Townsend[6,7], Lars S. Maier[4], and Céline Marionneau[1]

Phosphorylation of the voltage-gated Na^+ (Na_V) channel $Na_V1.5$ regulates cardiac excitability, yet the phosphorylation sites regulating its function and the underlying mechanisms remain largely unknown. Using a systematic, quantitative phosphoproteomic approach, we analyzed $Na_V1.5$ channel complexes purified from nonfailing and failing mouse left ventricles, and we identified 42 phosphorylation sites on $Na_V1.5$. Most sites are clustered, and three of these clusters are highly phosphorylated. Analyses of phosphosilent and phosphomimetic $Na_V1.5$ mutants revealed the roles of three phosphosites in regulating $Na_V1.5$ channel expression and gating. The phosphorylated serines S664 and S667 regulate the voltage dependence of channel activation in a cumulative manner, whereas the nearby S671, the phosphorylation of which is increased in failing hearts, regulates cell surface $Na_V1.5$ expression and peak Na^+ current. No additional roles could be assigned to the other clusters of phosphosites. Taken together, our results demonstrate that ventricular $Na_V1.5$ is highly phosphorylated and that the phosphorylation-dependent regulation of $Na_V1.5$ channels is highly complex, site specific, and dynamic.

Introduction

Voltage-gated Na^+ (Na_V) channels are key determinants of myocardial excitability, and defects in Na_V channel expression or functioning in the context of inherited or acquired cardiac disease increase the propensity to develop lethal arrhythmias (Remme and Bezzina, 2010). Ventricular Na_V channels, composed primarily of the $Na_V1.5$ channel pore-forming subunit, in association with several accessory/regulatory proteins, generate the transient peak Na^+ current (I_{Na}) responsible for the action potential upstroke and rapid intercellular conduction. While cardiac myocyte Na_V channels inactivate quickly, there is a finite probability (~0.5%) of channels remaining open, resulting in the late component of the Na^+ current (I_{NaL}), which contributes to determining action potential duration. In the ventricular myocardium, the $Na_V1.5$ protein is subject to many post-translational modifications, each of which fine-tunes channel expression and functioning in various physiological and disease contexts. Among the 11 different post-translational modifications previously shown to regulate cardiac $Na_V1.5$ channels, phosphorylation at serine, threonine, and tyrosine residues is certainly the best characterized (reviewed in Marionneau and Abriel, 2015; Pei et al., 2016; Yu et al., 2018; Plant et al., 2020).

A role for phosphorylation in regulating cardiac $Na_V1.5$ channels was first suggested in a pioneering study demonstrating that β-adrenergic receptors couple to Na_V channels not only through a direct G protein pathway but also through an indirect PKA-dependent pathway (Schubert et al., 1989). The involvement of several additional kinases and phosphatases in regulating I_{Na} and/or I_{NaL} later spotlighted the functional relevance of cardiac $Na_V1.5$ channel phosphorylation. Perhaps most strikingly, progress in mass spectrometry (MS)-based phosphoproteomic analyses recently buttressed the field by revealing the existence of multiple phosphorylation sites on native ventricular (Marionneau et al., 2012b; Burel et al., 2017) and heterologously expressed (Herren et al., 2015) $Na_V1.5$ channels. Yet, little is known about the roles and detailed molecular mechanisms that underlie phosphorylation-dependent regulation of cardiac $Na_V1.5$ channels.

[1]Université de Nantes, Centre national de la recherche scientifique, Institut National de la Santé et de la Recherche Médicale, l'Institut du thorax, Nantes, France; [2]Department of Biomedical Engineering, Washington University in Saint Louis, St. Louis, MO; [3]Bioinformatics Solutions Inc., Waterloo, Ontario, Canada; [4]Department of Internal Medicine II, University Heart Center, University Hospital Regensburg, Regensburg, Germany; [5]Department of Developmental Biology, Washington University Medical School, St. Louis, MO; [6]Department of Medicine, Washington University Medical School, St. Louis, MO; [7]Department of Cell Biology and Physiology, Washington University Medical School, St. Louis, MO.

Correspondence to Céline Marionneau: celine.marionneau@univ-nantes.fr.

Phosphorylation of $Na_V1.5$ channels has also recently been suggested as an arrhythmogenic mechanism in heart failure (Wagner et al., 2006; Maltsev et al., 2008; Koval et al., 2012; Aiba et al., 2013; Toischer et al., 2013; Glynn et al., 2015). The Na_V channel defects associated with heart failure are most often characterized by increased I_{NaL} and/or decreased I_{Na}, contributing to action potential prolongation and conduction slowing, respectively (Zicha et al., 2004; Valdivia et al., 2005; Maltsev et al., 2007; Xi et al., 2009; Aiba et al., 2013; Toischer et al., 2013). The increase in I_{NaL} has reportedly been linked to the activation of kinases, mainly the Ca^{2+}/calmodulin-dependent protein kinase II (CaMKII; Wagner et al., 2006; Maltsev et al., 2008; Aiba et al., 2013; Toischer et al., 2013), and several studies have focused on identifying the CaMKII-dependent $Na_V1.5$ phosphorylation sites (Hund et al., 2010; Ashpole et al., 2012; Herren et al., 2015; Burel et al., 2017). Notably, increased CaMKII-dependent $Na_V1.5$ phosphorylation at serine 571 has been reported and suggested to increase I_{NaL} in nonischemic human heart failure (Koval et al., 2012) and in animal models of heart disease (Koval et al., 2012; Toischer et al., 2013; Glynn et al., 2015). Nevertheless, $Na_V1.5$ channel phosphorylation may not be the sole mechanism involved in the observed pathophysiological defects, as other evidence suggests roles for up-regulation of the neuronal $Na_V1.1$ (Xi et al., 2009; Mishra et al., 2015), $Na_V1.6$ (Xi et al., 2009), or $Na_V1.8$ (Dybkova et al., 2018) channels. Intensive investigations were also undertaken to understand the causes of the reduced I_{Na}; yet, the detailed underlying molecular mechanisms remain unclear. While most studies failed to detect any changes in $Na_V1.5$ transcript or total protein expression in failing human hearts (Kääb et al., 1998) or in animal models of heart failure (Zicha et al., 2004; Valdivia et al., 2005), several mechanisms have been suggested to contribute to reduced I_{Na}, including the generation of a C-terminal truncation splicing variant switch in $Na_V1.5$ transcripts (Shang et al., 2007; Noyes et al., 2017), elevated NADH and reactive oxygen species production (Liu et al., 2013), or increased intracellular Ca^{2+} concentration and subsequent increased expression of the E3 ubiquitin ligase Nedd4-2 (Luo et al., 2017). In line with reduced I_{Na}, a recent study using high-resolution imaging and functional techniques showed a reduction in $Na_V1.5$ cluster size and a corresponding decreased number of open channels at the lateral membranes of ventricular myocytes from mice subjected to transverse aortic constriction (TAC), without any changes in $Na_V1.5$ transcript or total protein expression (Rivaud et al., 2017).

In this study, we investigated the patterns of phosphorylation of native mouse left ventricular $Na_V1.5$ channels and the roles of identified phosphorylation sites in regulating $Na_V1.5$ channel expression and functioning. Using quantitative MS-based phosphoproteomic analyses, we identified and quantified in situ the native phosphorylation sites of the $Na_V1.5$ in a mouse model of pressure overload–induced heart failure produced by TAC. By analyzing the expression and the functional properties of phosphosilent and phosphomimetic $Na_V1.5$ mutant channels in human embryonic kidney 293 (HEK-293) cells, as well as simulating the consequences of phosphorylation on $Na_V1.5$ peptide segment expansion, we identified phosphorylation hot spots for regulation of both channel cell surface expression and gating.

Materials and methods

Statement on the use of murine tissue

All investigations conformed to Directive 2010/63/EU of the European Parliament, to the Guide for the Care and Use of Laboratory Animals published by the National Institutes of Health (Publication No. 85-23, revised 1985), and to local institutional guidelines.

Animal model of heart failure

Heart failure was induced by TAC as described previously (Toischer et al., 2013). 8-wk-old male C57BL/6J mice were anesthetized using intraperitoneal injections of medetomidine (0.5 mg/kg), midazolam (5 mg/kg), and fentanyl (0.05 mg/kg body weight). A horizontal incision (1–1.5 cm) at the jugulum was used to display the transverse aorta, and a 27-gauge needle was tied against the aorta using a 6-0 nonabsorbable suture. After removal of the 27-gauge needle, the skin was closed, and the mice were kept on a heating plate until they recovered from the anesthesia. Sham animals underwent the same procedure except for the banding of the transverse aorta. At the end of the surgery, anesthesia was antagonized using intraperitoneal injections of atipamezole (2.5 mg/kg), flumazenil (0.5 mg/kg), and buprenorphine (0.1 mg/kg body weight). For analgesia, metamizole (1.33 mg/ml) was added to the drinking water 2 d before surgery and was supplied for 7 d after operation. In addition, buprenorphine (60 µg/kg body weight) was administered subcutaneously 1 h before surgery. A TAC with a mean gradient of <5 mm Hg was deemed insufficient to induce heart failure, and if observed, the animal was excluded from later analysis. Mice were sacrificed 5 wk after TAC by cervical dislocation, and left ventricles were harvested, flash frozen, and stored for further analyses.

Mouse echocardiography

Transthoracic echocardiography was performed blinded before and 5 wk after TAC using a Vevo 3100 system (VisualSonics) equipped with a 30-MHz center frequency transducer, as described previously (Toischer et al., 2013). The animals were initially anesthetized with 3% isoflurane, while temperature-, respiration-, and electrocardiogram-controlled anesthesia was maintained with 1.5% isoflurane. 2-D cine loops with frame rates of >200 frames/s of a long-axis view and a short-axis view at the midlevel of the papillary muscles, as well as M-mode loops of the short-axis view, were recorded. Thicknesses of the anterior and posterior walls of the left ventricle, the inner diameter of the left ventricle (LVID), and the area of the left ventricular cavity were measured in systole and diastole from the short-axis view according to standard procedures (Gao et al., 2011). Maximal left ventricular length was measured from the long-axis view. Systolic and diastolic left ventricular volumes were calculated using the area-length method, and the ejection fraction was derived. Left ventricular mass (LVM) was calculated from anterior and posterior wall thicknesses using Vevo LAB Software (VisualSonics).

Pulsed-wave Doppler ultrasound was used to assess mean gradients 3 d after the TAC procedure.

Immunoprecipitation (IP) of Na_V channel complexes

Flash-frozen left ventricles from four sham and five TAC mice were homogenized individually in ice-cold lysis buffer containing 20 mM HEPES (pH 7.4), 150 mM NaCl, 0.5% amidosulfobetaine, 1× complete protease inhibitor cocktail tablet, 1 mM PMSF, 0.7 µg/ml pepstatin A (Thermo Fisher Scientific), and 1× Halt phosphatase inhibitor cocktail (Thermo Fisher Scientific) as described previously (Marionneau et al., 2012b). All reagents were from Sigma-Aldrich unless otherwise noted. After 15-min rotation at 4°C, 8 mg of the soluble protein fractions were precleared with 200 µl of protein G-magnetic Dynabeads (Thermo Fisher Scientific) for 1 h and subsequently used for IPs with 48 µg of an anti-Na_VPAN mouse mAb (mαNa_VPAN, S8809; Sigma-Aldrich) raised against the SP19 epitope (Vassilev et al., 1988) located in the third intracellular linker loop and common to all Na_V channel pore-forming subunits. Prior to the IP, antibodies were cross-linked to 200 µl of protein G-magnetic Dynabeads using 20 mM dimethyl pimelimidate (Thermo Fisher Scientific; Schneider et al., 1982). Protein samples and antibody-coupled beads were mixed for 2 h at 4°C. Magnetic beads were then collected and washed rapidly four times with ice-cold lysis buffer, and isolated protein complexes were eluted from the beads in 1× SDS sample buffer (Bio-Rad Laboratories) at 60°C for 10 min. 99% of the immunoprecipitated mouse left ventricular Na_V channel protein complexes were analyzed by MS, and the remaining 1% were used to verify IP yields by Western blotting using a rabbit polyclonal anti-Na_V1.5 antibody (RbαNa_V1.5, 1:1,000, ASC-005; Alomone Laboratories).

Peptide preparation and isobaric labeling for liquid chromatography (LC)-MS

The IP eluates were thawed on ice, reduced, and denatured by heating for 10 min at 95°C. The Cys residues were alkylated with iodoacetamide (10 mM) for 45 min at room temperature in the dark. The peptides were prepared using a modification (Erde et al., 2014) of the filter-aided sample preparation method (Wiśniewski et al., 2009). After the addition of 300 µl of 100 mM Tris buffer (pH 8.5) containing 8 M urea (UT buffer) and vortexing, the samples were transferred to YM-30 filter units (MRCF0R030; EMD Millipore) and spun for 14 min at 10,000 rcf (model 5424; Eppendorf). The filters were washed with 200 µl of UT buffer, and the spin-wash cycle was repeated twice. The samples were then exchanged into digest buffer with the addition of 200 µl of 50 mM Tris buffer, pH 8.0, followed by centrifugation (10,000 rcf for 10 min). After transferring the upper filter units to new collection tubes, 80 µl of digest buffer were added, and the samples were digested with trypsin (1 µg) for 4 h at 37°C. The digestion was continued overnight after adding another aliquot of trypsin. The filter units were then spun for 10 min (10,000 rcf) in an Eppendorf microcentrifuge. The filter was washed with 50 µl of Tris buffer (100 mM, pH 8.0), followed by centrifugation. The digests were extracted three times with 1 ml ethyl acetate and acidified to 1% trifluoroacetic acid (TFA) using a 50% aqueous solution. The pH was <2.0 by checking with pH paper. The solid-phase extraction of the peptides was performed using porous graphite carbon microtips (Chen et al., 2012). The peptides were eluted with 60% acetonitrile in 0.1% TFA and pooled for drying in a Speed-Vac (model Savant DNA 120 concentrator; Thermo Fisher Scientific) after adding TFA to 5%. The peptides were dissolved in 20 µl of 1% acetonitrile in water. An aliquot (10%) was removed for quantification using the Pierce Quantitative Fluorometric Peptide Assay Kit (23290; Thermo Fisher Scientific). The remainder of the peptides from each IP sample (~0.5–3.5 µg) and 1.16 µg of reference pool peptide were transferred into a new 0.5-ml Eppendorf tube, dried in the Speed-Vac, and dissolved in 12 µl HEPES buffer (100 mM, pH 8.0, H3537; Sigma-Aldrich).

The samples were labeled with tandem mass tag (TMT) reagents (TMT11; Thermo Fisher Scientific) according to the manufacturer's protocol. The labeled samples were pooled, dried, and resuspended in 120 µl of 1% formic acid (FA). The TMT11-labeled sample was desalted as described above for the unlabeled peptides. The eluates were transferred to autosampler vials (200046; SUN-SRi), dried, and stored at −80°C for capillary LC interfaced to a mass spectrometer (nanoscale LC-MS).

Nanoscale LC-MS

The samples in FA (1%) were loaded (2.5 µl) onto a 75-µm ID × 50-cm Acclaim PepMap 100 C18 RSLC column (Thermo Fisher Scientific) on an EASY nano-LC (Thermo Fisher Scientific). The column was equilibrated using constant pressure (700 bar) with 20 µl of solvent A (0.1% FA). The peptides were eluted using the following gradient program with a flow rate of 300 nl/min and using solvents A and B (acetonitrile with 0.1% FA): solvent A containing 5% B for 1 min, increased to 25% B over 87 min, to 35% B over 40 min, to 70% B in 6 min and constant 70% B for 6 min, to 95% B over 2 min and constant 95% B for 18 min. The data were acquired in data-dependent acquisition mode. The mass spectrum of peptide precursors (MS1) scans were acquired with the Orbitrap mass analyzer over mass-to-charge ratio = 375–1,500 and with resolution set to 70,000. 12 data-dependent high-energy collisional dissociation spectra (MS2) were acquired from each MS1 scan with a mass resolving power set to 35,000, a range of mass-to-charge ratio = 100–1,500, an isolation width of 2 Th, and a normalized collision energy setting of 32%. The maximum injection time was 60 ms for parent ion analysis and 120 ms for product ion analysis. The ions that were selected for MS2 were dynamically excluded for 20 s. The automatic gain control was set at a target value of 3e6 ions for MS1 scans and 1e5 ions for MS2. Peptide ions with charge states of 1 or ≥7 were excluded for higher-energy collision–induced dissociation acquisition.

MS data analysis

Peptide identification from raw MS data was performed using PEAKS Studio 8.5 (Bioinformatics Solutions Inc.; Zhang et al., 2012). The Uni-mouse-Reference-20131008 protein database was used for spectral matching. The precursor and product ion mass tolerances were set to 20 ppm and 0.05 D, respectively, and the enzyme cleavage specificity was set to trypsin, with a maximum of three missed cleavages allowed. Carbamidomethylation

(Cys) and TMTs (Lys and/or peptide N terminus) were treated as fixed modifications, while oxidation (Met), pyroglutamination (Gln), deamidation (Asn and/or Gln), methylation (Lys and/or Arg), dimethylation (Lys and/or Arg), acetylation (Lys), and phosphorylation (Ser, Thr, and/or Tyr) were considered variable modifications. The definitive annotation of each $Na_V1.5$ phosphopeptide–spectrum match was obtained by manual verification and interpretation. The phosphorylation site assignments were based on the presence or absence of the unphosphorylated and phosphorylated b and y ions flanking the site(s) of phosphorylation, ions referred to as "site-discriminating ions" throughout this study. When site-discriminating ions were not all detected, the assignment of phosphorylation sites was narrowed down to several possibilities by elimination (for example, pS1056 and/or pT1058). Representative MS/MS spectra, PEAKS −10lgP scores, mass errors of parent ions (in ppm), and charge state confirmations of site-discriminating b and y ions are presented in Table 2, Table S3, and Data S1.

The protein and peptide relative abundances in TAC versus sham mαNa_VPAN-IPs were calculated using quantification of TMT reporter ions. Reporter ion intensities in each TMT channel were normalized to the mean reporter ion intensities of $Na_V1.5$-derived peptides (normalization to spike) to correct for differences in IP yields and technical variabilities. Normalization factors are presented in Fig. S1 B. Quantification values of each peptide–spectrum match were exported into Excel, and the mean peptide abundance ratios were calculated from the abundance ratios of all manually verified peptide–spectrum matches assigning to the phosphorylation site(s) of interest. Label-free quantitative analysis of the areas of extracted MS1 chromatograms of phosphorylated and nonphosphorylated peptide ions covering the phosphorylation site(s) of interest was used to evaluate the proportion of phosphorylated to nonphosphorylated peptides at each position, as well as the relative abundances of phosphopeptides.

Plasmids

The $Na_V1.5$ phosphomutant constructs were generated by mutating the serine(s)/threonine(s) to alanine(s) (A) or glutamate (E), as well as aspartate(s) (D) in the $Na_V1.5$-S664-671D quadruple phosphomimetic channel, by site-directed mutagenesis of a pCI-$Na_V1.5$ plasmid containing the human $Na_V1.5$ hH1C cDNA (Makielski et al., 2003; National Center for Biotechnology Information reference sequence NM_000335) using the QuikChange II XL Site-Directed Mutagenesis Kit (Agilent) or the Q5 Site-Directed Mutagenesis Kit (New England Biolabs). The mutated constructs were then digested with restriction endonucleases to excise the mutated fragments, which were then subcloned into the original pCI-$Na_V1.5$ plasmid. The human $Na_V\beta1$ (NM_001037; a gift from A.L. George, Department of Pharmacology, Northwestern University, Evanston, IL) cDNAs were subcloned into pRc/cytomegalovirus. All constructs were sequenced to ensure that no unintentional mutations were introduced.

Culture and transient transfections

HEK-293 cells were maintained in Dulbecco's modified Eagle's medium (Thermo Fisher Scientific), supplemented with 10% FBS, 100 U/ml penicillin, and 100 µg/ml streptomycin in a 37°C, 5% CO_2, 95% air incubator. Cells were transiently transfected at 70–80% confluence in 35-mm dishes with 0.6 µg of the WT or phosphomutant $Na_V1.5$ plasmid and 1.2 µg of the $Na_V\beta1$ plasmid using 2 µl Lipofectamine 2000 (Thermo Fisher Scientific) following the manufacturer's instructions. For whole-cell recordings, transfections also contained 0.2 µg of the pEGFP plasmid (enhanced GFP plasmid; Clontech), and EGFP expression served as a marker of transfection. The absolute amounts of the various constructs were calculated, and the empty pcDNA3.1 plasmid was used as a filler plasmid to keep the total DNA constant at 2 µg in each transfection.

Electrophysiological recordings

Whole-cell Na_V currents were recorded at room temperature from transiently transfected HEK-293 cells using an Axopatch 200A amplifier (Axon Instruments/Molecular Devices) 48 h after transfection. Voltage-clamp protocols were applied using the pClamp 10.2 software package (Axon Instruments) interfaced to the electrophysiological equipment using a Digidata 1440A digitizer (Axon Instruments). Current signals were filtered at 10 kHz before digitization at 50 kHz and storage. Patch-clamp pipettes were fabricated from borosilicate glass (OD, 1.5 mm; ID, 0.86 mm; Sutter Instrument) using a P-97 micropipette puller (Sutter Instrument), coated with wax, and fire polished to a resistance between 1.5 and 2.5 MΩ when filled with internal solution. The internal solution contained (in mM) 5 NaCl, 115 CsF, 20 CsCl, 10 HEPES, and 10 EGTA (pH 7.35 with CsOH, ∼300 mosM). The external solution contained (in mM) 10 NaCl (20 NaCl for analysis of single phosphomutants), 103 CsCl, 25 TEA-Cl, 10 HEPES, 5 glucose, 1 $CaCl_2$, and 2 $MgCl_2$ (pH 7.4 with CsOH, ∼300 mosM). All chemicals were purchased from Sigma-Aldrich. After establishing the whole-cell configuration, 3 min were allowed to ensure stabilization of voltage-dependence of activation and inactivation properties, at which time 25-ms voltage steps to ±10 mV from a holding potential (HP) of −70 mV were applied to allow measurement of whole-cell Cm, input, and series resistances. Only cells with access resistance <7 MΩ were used, and input resistances were typically >5 GΩ. After compensation of series resistance (80%), the membrane was held at an HP of −120 mV, and the voltage-clamp protocols were performed as indicated below. Leak currents were always <200 pA at HP (−120 mV) and were corrected offline. Cells exhibiting peak current amplitudes <500 or >5,000 pA were excluded from analyses of biophysical properties because of leak or voltage-clamp issues, respectively, but were conserved in analyses of peak current density to avoid bias in evaluation of current densities.

Data were compiled and analyzed using ClampFit 10.2 (Axon Instruments), Microsoft Excel, and Prism (GraphPad Software). Whole-cell Cm values were determined by analyzing the decays of capacitive transients elicited by brief (25-ms) voltage steps to ±10 mV from the HP (−70 mV). Input resistances were calculated from the steady-state currents elicited by the same ±10-mV steps (from the HP). Series resistances were calculated by dividing the decay time constants of the capacitive transients (fitted with single exponentials) by the Cm. To determine peak Na^+ I-V

relationships, currents were elicited by 50-ms depolarizing pulses to potentials ranging from −80 to +40 mV (presented at 5-s intervals in 5-mV increments) from an HP of −120 mV. Peak current amplitudes were defined as the maximal currents evoked at each voltage. Current amplitudes were leak corrected and normalized to the Cm, and current densities are presented.

To analyze voltage dependence of current activation properties, G values were calculated, and G-V relationships were fitted with the Boltzmann equation $G = G_{max}/\{1 + \exp[-(V_m - V_{1/2}) / k]\}$, in which $V_{1/2}$ is the membrane potential of half-activation and k is the slope factor. The time courses of inactivation of macroscopic currents were fitted with biexponential functions, $I(t) = A_{fast} \times \exp(-t/\tau_{fast}) + A_{slow} \times \exp(-t/\tau_{slow}) + A_0$, in which A_{fast} and A_{slow} are the amplitudes of the fast and slow inactivating current components, respectively, and τ_{fast} and τ_{slow} are the decay time constants of A_{fast} and A_{slow}, respectively. A standard two-pulse protocol was used to examine the voltage dependences of steady-state inactivation. From an HP of −120 mV, 1-s conditioning pulses to potentials ranging from −120 to −45 mV (in 5-mV increments) were followed by 20-ms test depolarizations to −20 mV (interpulse intervals were 5 s). Current amplitudes evoked from each conditioning voltage were measured and normalized to the maximal current (I_{max}) evoked from −120 mV, and normalized currents were plotted as a function of the conditioning voltage. The resulting steady-state inactivation curves were fitted with the Boltzmann equation $I = I_{max}/\{1 + \exp[(V_m - V_{1/2}) / k)]\}$, in which $V_{1/2}$ is the membrane potential of half-inactivation and k is the slope factor. To examine the rates of recovery from inactivation, a three-pulse protocol was used. Cells were first depolarized to −20 mV (from an HP of −120 mV) to inactivate the channels and subsequently repolarized to −120 mV for varying times (ranging from 1 to 200 ms), followed by test depolarizations to −20 mV to assess the extent of recovery (interpulse intervals were 5-s). The current amplitudes at −20 mV, measured following each recovery period, were normalized to the maximal current amplitude and plotted as a function of the recovery time. The resulting plot was fitted with a single exponential function $I(t) = A \times [1 - \exp(-t/\tau_{rec})]$ to determine the recovery time constant. For each of these biophysical properties, data from individual cells were first fitted and then averaged.

The currents generated on expression of each phosphosilent and phosphomimetic $Na_V1.5$ mutant were recorded and compared with currents generated by the $Na_V1.5$-WT construct obtained on the same days of patch-clamp analyses. The densities and properties of $Na_V1.5$-WT currents in each dataset were similar, and, for the sake of clarity, a single representative $Na_V1.5$-WT channel dataset was chosen and presented in Fig. S3 and Tables 3 and 4.

In experiments aimed at recording the tetrodotoxin (TTX)-sensitive I_{NaL}, cells were bathed in external solution containing (in mM) 120 NaCl, 25 TEA-Cl, 10 HEPES, 5 glucose, 1 $CaCl_2$, and 2 $MgCl_2$ (pH 7.4 with CsOH, ∼300 mosM). Repetitive 350-ms test pulses to −20 mV from an HP of −120 mV (at 5-s intervals) were applied to cells to record I_{Na} in the absence of TTX. Cells were then superfused locally with the external solution supplemented with 30 µM TTX (Bio-Techne SAS). Only cells exhibiting peak current amplitudes >4,000 pA were used (those with peak currents <4,000 pA did not show measurable I_{NaL}), and cells with difference in leak current amplitudes before and after TTX application >5 pA at −20 mV (calculated from leak currents at −120 mV) were excluded from analyses. TTX-sensitive currents from individual cells were determined by offline digital subtraction of average leak-subtracted currents obtained from five recordings in the absence and in the presence of TTX after achieving steady state. The amplitude of TTX-sensitive I_{NaL} was defined as the steady-state current amplitude (A_0) obtained by fitting the inactivation decay of macroscopic TTX-sensitive current with the double-exponential function $I(t) = A_{fast} \times \exp(-t/\tau_{fast}) + A_{slow} \times \exp(-t/\tau_{slow}) + A_0$. For each cell, the TTX-sensitive I_{NaL} amplitude was normalized to the peak I_{Na} amplitude and expressed as a percentage of the peak I_{Na}.

Cell surface biotinylation and Western blot analyses

Surface biotinylation of HEK-293 cells was completed as described previously (Marionneau et al., 2012a). Briefly, cells were incubated with the cleavable EZ-Link Sulfo-NHS-SS-Biotin (0.5 mg/ml; Thermo Fisher Scientific) in ice-cold PBS (pH 7.4) for 30 min at 4°C. Free biotin was quenched with Tris-saline (10 mM Tris [pH 7.4], 120 mM NaCl), and detergent-soluble cell lysates were prepared. Biotinylated cell surface proteins were affinity purified using NeutrAvidin-conjugated agarose beads (Thermo Fisher Scientific), and purified cell surface proteins were analyzed by Western blot using the mαNa_VPAN antibody (1:2,000, S8809; Sigma-Aldrich), the anti-transferrin receptor mouse mAb (TransR, 1:1000, Thermo Fisher Scientific), and the anti-glyceraldehyde 3-phosphate dehydrogenase mouse mAb (anti-GAPDH, 1:100,000; Santa Cruz Biotechnology). Bound primary antibodies were detected using horseradish peroxidase–conjugated goat anti-mouse secondary antibodies (Cell Signaling Technology), and protein signals were visualized using the SuperSignal West Dura Extended Duration Substrate (Thermo Fisher Scientific). Bands corresponding to $Na_V1.5$ were normalized to bands corresponding to TransR from the same sample. $Na_V1.5$ phosphomutant protein expression (total or cell surface) is expressed relative to $Na_V1.5$-WT protein expression (total or cell surface).

Molecular simulations

Molecular simulations were performed with the CAMPARI software package (Vitalis and Pappu, 2009b) using the ABSINTH implicit solvation model (Vitalis and Pappu, 2009a) and parameters from the all-atom optimized potentials for liquid simulations force field. Markov chain Metropolis Monte Carlo moves sampled the conformational space of each protein segment. To mimic a 5 mM NaCl concentration, neutralizing and excess Na^+ and Cl^- ions were modeled explicitly with the protein segments in spherical droplets of (5 × number of residues) Å radius. 10 simulation runs were performed for each sequence construct, and the average of these 10 runs was then plotted. The simulations denoted as EV (excluded volume) and FRC (Flory random coil) are reference models. In the EV limit, the only interactions considered are the pairwise repulsions. In the FRC

limit, conformations are constructed by randomly sampling residue-specific backbone dihedral angles. Three EV and three FRC simulation runs were performed for each protein segment, and the averages were plotted.

Statistical analyses

Results are expressed as means ± SEMs. Data were first tested for normality using the D'Agostino and Pearson normality test. Depending on the results of normality tests, statistical analyses were then performed using the Mann-Whitney nonparametric test, Kruskal-Wallis one-way ANOVA followed by Dunn's post-hoc test, or one-way ANOVA followed by Dunnett's post-hoc test, as indicated in figures and tables. All these analyses, as well as plots and graphs, were performed using Prism software (GraphPad Software).

Online supplemental material

The supplemental figures and tables show multiple pieces of raw or analyzed data to complement the main figures as explicated in the text. Fig. S1 shows IP yields and relative quantification of $Na_V1.5$ peptide abundances from sham and TAC mouse left ventricles. Fig. S2 shows conservation of phosphorylation sites in mouse and human $Na_V1.5$. Fig. S3 shows distributions and mean ± SEM membrane potentials for half-activation and half-inactivation, peak I_{Na} densities, and time constants of recovery from inactivation of WT and mutant $Na_V1.5$ channels. Fig. S4 shows distributions and mean ± SEM of TTX-sensitive I_{NaL} densities of quadruple S664-671 and simple S671 $Na_V1.5$ phosphomutants. Data S1 shows representative MS/MS spectra corresponding to the phosphopeptides enabling the best phosphorylation site assignment(s) for each phosphorylation site. Table S1 lists echocardiographic parameters of sham and TAC mice before and 5 wk after surgery. Table S2 summarizes $Na_V1.5$ phosphorylation sites identified in the present and previous studies. Table S3 lists phosphorylation sites, phosphopeptides, and site-discriminating ions identified in coimmunoprecipitated Na_V α subunits from sham and TAC mouse left ventricles using MS.

Results

Purification and characterization of Na_V channel complexes from sham and TAC mouse left ventricles

Na_V channel complexes from four sham-operated and five TAC mouse left ventricles were purified by IP using an mαNa_VPAN and characterized using quantitative isobaric TMT-based analysis. As illustrated in Table S1, and consistent with previous findings (Toischer et al., 2013), the echocardiographic analysis confirmed increased LVMs (LVM/body weight ratios), reduced ejection fractions, but unaltered left ventricular end-diastolic diameters (LVID;d) 5 wk after the TAC surgery, demonstrating left ventricular concentric hypertrophy and systolic contractile dysfunction or heart failure in the TAC animals. Western blot analyses of total lysates showed similar total $Na_V1.5$ protein expression in sham and TAC left ventricles, which resulted in similar $Na_V1.5$ IP yields in the nine samples (Fig. S1 A). Isolated Na_V channel complexes were then digested with trypsin, and peptide mixtures were labeled with different TMTs and combined in the same TMT set for multiplexed MS/MS analysis (Fig. 1 E). As illustrated in Table 1, the $Na_V1.5$ protein was the most represented protein in the mαNa_VPAN-IPs, with 310 unique and $Na_V1.5$-specific peptides identified and 56% amino acid sequence coverage (70% with the transmembrane domains removed; Fig. 2).

Consistent with the homogeneous yields in the $Na_V1.5$ IP, the relative abundance of the $Na_V1.5$ peptides detected by MS in the nine samples was similar and used for normalization of each single protein and peptide abundance (Fig. S1 B). Accordingly, the distribution of normalized abundance ratios of $Na_V1.5$ peptides (in log_2) in TAC versus sham mαNa_VPAN-IPs was centered on zero (Fig. S1 C). Altogether, therefore, these observations attest to a high reproducibility across biological replicates and a low technical variability inherent to experimental procedures. Of note, and as described previously (Makielski et al., 2003), several $Na_V1.5$ peptides differing by the presence (1079-QQESQVVSGGHEPPQEPR, Q1080 variant) or absence (1077-SKQESQVVSGGHEPPQEPR and 1078-KQESQVVSGGHEPPQEPR, Q1080del variant) of a glutamine (Q) at position 1080 were detected (Table 1 and Fig. 2), reflecting the expression of two distinct $Na_V1.5$ variants in adult mouse left ventricles; Q1080del corresponds to the commonly reported hH1C variant. The identification of additional, nondiscriminating peptides (1079-QESQVVSGGHEPPQEPR and 1079-QESQVVSGGH), which could arise from either variant, however, prevented us from quantifying the relative abundance of the two $Na_V1.5$ variants. These analyses also allowed the identification of eight additional Na_V channel pore-forming subunits, among which $Na_V1.4$ is the most abundant, with 86 unique $Na_V1.4$-specific peptides detected (Table 1). In addition, several previously identified $Na_V1.5$ channel associated/regulatory proteins, including calmodulin, the VY variant of fibroblast growth factor homologous factor 2 (FHF2-VY) and ankyrin-G, were detected, with no significant differences in abundance between sham and TAC mαNa_VPAN-IPs (Table 1).

Identification and quantification of 42 $Na_V1.5$ phosphorylation sites in sham and TAC mouse left ventricles

The phosphoproteomic analysis of the mαNa_VPAN-IPs from sham and TAC mouse left ventricles allowed the unambiguous identification of 42 native phosphorylation sites in the $Na_V1.5$ protein, 19 of which have never, to our knowledge, been previously described (Figs. 1 A and 2). Table 2 lists the phosphopeptides enabling the best phosphorylation site assignment(s) for each phosphorylation site, and corresponding MS/MS spectra are presented in Data S1. Table S2 lists these 42 phosphorylation sites with all the other phosphorylation sites identified so far on the mouse and/or human $Na_V1.5$ protein, whether by using MS, in silico, and/or in vitro analyses. Interestingly, the vast majority of these 42 phosphorylation sites are clustered, with the first intracellular linker loop of $Na_V1.5$ revealed as a hot spot for phosphorylation, with a total of 21 sites identified. Further label-free quantitative analysis of the areas of extracted MS1 peptide ion chromatograms revealed large differences in the relative abundance of the individual

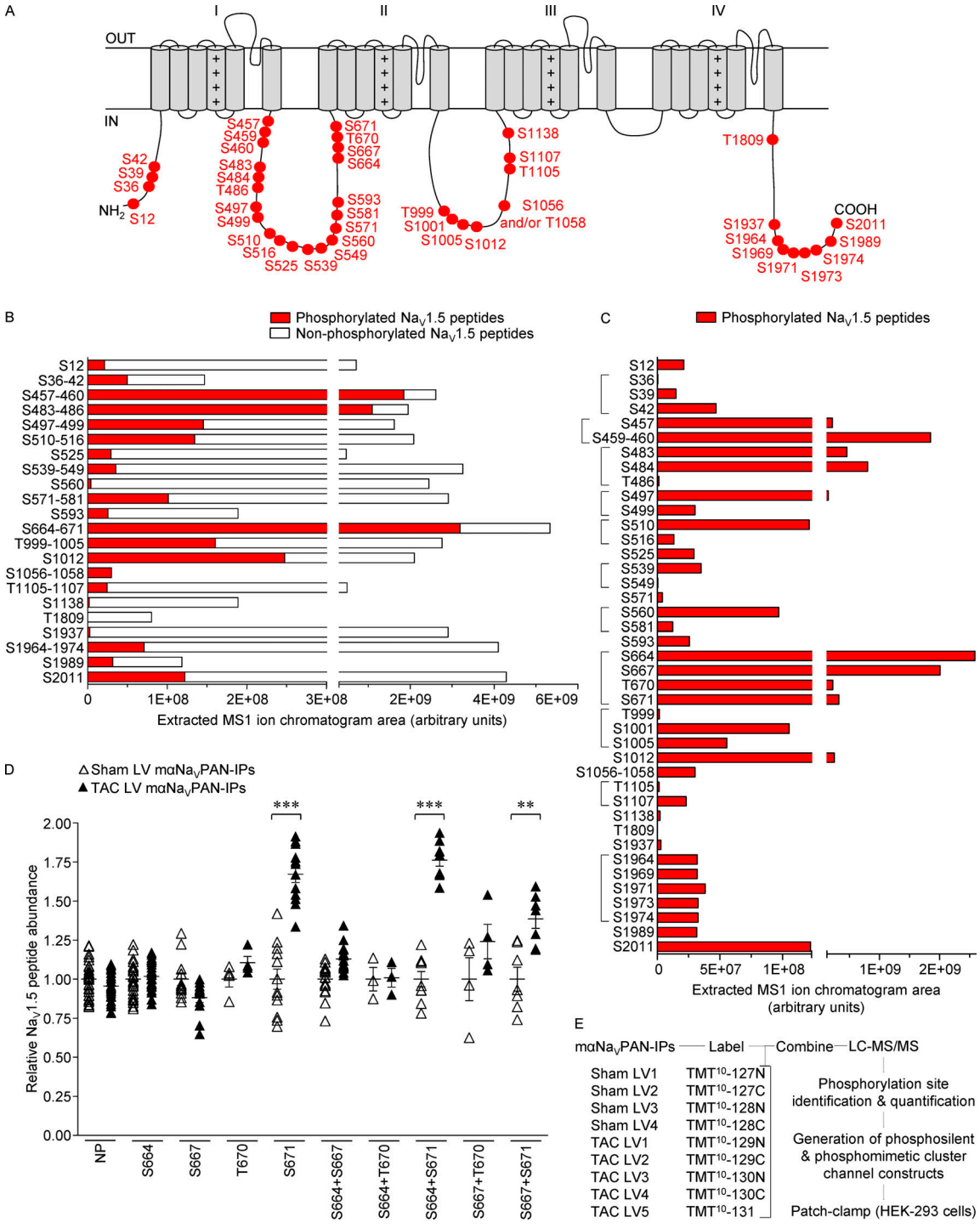

Figure 1. **Localization and quantification of 42 MS-identified $Na_V1.5$ phosphorylation sites in mαNa_VPAN-IPs from sham and TAC mouse left ventricles (LVs). (A)** Schematic representation of phosphorylation sites on the $Na_V1.5$ protein (UniProt reference sequence K3W4N7). Two phosphorylation site locations are possible at amino acids S1056-T1058. **(B)** The areas of extracted MS1 ion chromatograms, corresponding to MS2 spectra assigning phosphorylated (in red) and nonphosphorylated (in white) $Na_V1.5$ peptides at indicated phosphorylation site(s), in mαNa_VPAN-IPs from sham and TAC LVs are indicated. No red color is visible for the phosphorylated peptide at position T1809, because this phosphopeptide area is very small (area = 80,291 arbitrary unit) relative to the areas of the nonphosphorylated peptides (areas = 80,060,220 arbitrary unit). **(C)** The areas of extracted MS1 ion chromatograms, corresponding to MS2 spectra assigning phosphorylated peptides at indicated phosphorylation site(s), in mαNa_VPAN-IPs from sham and TAC LVs are indicated. The brackets indicate the subgroups of phosphorylation sites analyzed in B. Independent quantification of S459 and S460 phosphorylated peptides was not possible, because localization of the phosphorylation site in most of the phosphorylated peptides could not be discriminated. Similar to B, no red bar is visible for the phosphorylated peptide at position T1809, because this phosphopeptide area is very small (area = 80,291 arbitrary unit), relative to the areas of the other phosphorylated peptides. **(D)** Distributions and mean ± SEM relative abundances of individual $Na_V1.5$ phosphopeptides allowing assignments of indicated phosphorylation site(s), as well as of corresponding nonphosphorylated (NP) peptides, in TAC LV (n = 5, in black) versus sham LV (n = 4, in white)

mαNa$_V$PAN-IPs were obtained using TMT reporter ion intensities. The relative abundances of Na$_V$1.5 phosphopeptides exhibiting phosphorylation(s) on serine 671 (S671; *n* = 12 peptides) alone or in combination with serine 664 (S664 + S671; *n* = 9 peptides) or serine 667 (S667 + S671; *n* = 7 peptides) are increased (**, P < 0.01; ***, P < 0.001; Mann-Whitney test) in TAC LV versus sham LV mαNa$_V$PAN-IPs. **(E)** Experimental workflow used in the study. Once immunoprecipitated using the mαNa$_V$PAN antibodies, the Na$_V$ channel complexes from sham and TAC mouse LVs were labeled individually with different TMT^{10} tags and combined in the same TMT set for multiplexed LC-MS/MS analysis. Na$_V$1.5 phosphorylation sites were identified, quantified, and analyzed by clusters in whole-cell voltage-clamp recordings in HEK-293 cells.

phosphopeptides and the existence of three highly phosphorylated clusters at positions S457-S460, S483-T486, and S664-S671 (Fig. 1 B). In addition, and in contrast to the other phosphorylation sites, the phosphorylated peptides assigning these three phosphorylation clusters are more abundant than their nonphosphorylated counterparts, suggesting that these sites are mostly phosphorylated in native Na$_V$1.5 channels in WT mouse left ventricles. Looking into the detailed quantification of single phosphorylation sites inside each of these clusters, however, major differences in phosphopeptide abundance are evident (Fig. 1 C). This is the case, for example, of phosphorylation at S664 or S667, which is ∼10-fold more abundant than at residues T670 or S671.

To determine whether phosphorylation of Na$_V$1.5 is regulated in heart failure, the relative abundance of each Na$_V$1.5 phosphopeptide in TAC versus sham mαNa$_V$PAN-IPs was calculated using the relative abundance of TMT reporter ions. As illustrated in Fig. 1 D, peptides exhibiting phosphorylation(s) on serine 671 (S671) alone or in combination with serine 664 (S664 + S671) or serine 667 (S667 + S671) are significantly more abundant in the TAC than in the sham mαNa$_V$PAN-IPs. The relative abundance of their nonphosphorylated counterparts, however, is similar in sham and TAC mαNa$_V$PAN-IPs. None of the other Na$_V$1.5 phosphopeptides showed any significant differences in the sham and TAC mαNa$_V$PAN-IPs (Table 2). In addition to Na$_V$1.5, four phosphorylation sites on Na$_V$1.4 and one on Na$_V$1.3 could also be detected (Table S3 and Data S1). Taken together, these quantitative phosphoproteomic analyses identified 42 native phosphorylation sites on Na$_V$1.5, among which 3 clusters of phosphorylation in the first loop of the channel are highly phosphorylated in mouse left ventricles and one serine at position 671 shows increased phosphorylation in TAC mouse left ventricles.

Functional mapping of Na$_V$1.5 channel phosphorylation clusters

The identification of several clusters of phosphorylation sites on Na$_V$1.5 suggests that these sites may be involved in the coordinated regulation of channel expression and/or function. Of the eight clusters of phosphorylation identified in the mouse Na$_V$1.5 protein, seven are conserved in the human Na$_V$1.5 protein sequence; only the mouse T1105 is not conserved (Fig. S2). To investigate the functional roles of these (seven) phosphorylation clusters, phosphosilent and phosphomimetic Na$_V$1.5 channel constructs in the human Na$_V$1.5 hH1C cDNA sequence were generated, transiently expressed with the Na$_V$β1 channel subunit in HEK-293 cells, and characterized in whole-cell voltage-clamp recordings. In the phosphosilent constructs, mutations were introduced to replace serines/threonines (S/T) with alanines (A), whereas in the phosphomimetic constructs, mutations were introduced to substitute glutamates (E) for serines/threonines, to mimic phosphorylation.

As illustrated in Fig. 3 B, these whole-cell voltage-clamp analyses demonstrated that the voltage dependence of activation of the Na$_V$1.5-S664-671A quadruple phosphosilent channels, in which all four of S664, S667, T670, and S671 are mutated to alanines, is significantly (P < 0.001) shifted toward depolarized potentials compared with WT channels (see distributions, detailed properties, and statistics in Fig. S3 A and Table 3). The activation curve of the Na$_V$1.5-S664-671E quadruple phosphomimetic channel was also significantly (P < 0.001) shifted, although to a lesser extent, when compared with the phosphosilent channel. Together, therefore, these findings suggest that the S664-671 cluster is phosphorylated in HEK-293 cells and that disruption of phosphorylation at these sites shifts the voltage dependence of channel activation toward depolarized potentials. To further support the role of phosphorylation in this effect, the quadruple aspartate (D) phosphomimetic channel, Na$_V$1.5-S664-671D, was generated, and analysis of voltage dependence of channel activation demonstrated no differences when compared with the WT channel (Fig. 3 B, Fig. S3 A, and Table 3). Consequent to these effects, the time to peak I_{Na} (Fig. 3 D), as well as the inactivation time constants, τ_{fast} and τ_{slow} (Fig. 3, E and F), of the Na$_V$1.5-S664-671A and Na$_V$1.5-S664-671E quadruple phosphomutant channels were shifted toward depolarized potentials compared with the WT Na$_V$1.5 and the Na$_V$1.5-S664-671D quadruple phosphomimetic channels, until reaching full activation at ∼0 mV. In addition, the peak I_{Na} density of the Na$_V$1.5-S664-671E quadruple phosphomimetic channel was significantly (P < 0.05 at −20 mV) reduced compared with the WT channel, whereas no significant changes were observed with the Na$_V$1.5-S664-671A and Na$_V$1.5-S664-671D quadruple phosphomutant channels (Fig. 3 C; see distributions at −20 mV and statistics in Fig. S3 B and Table 3). Importantly, however, evaluation and comparison of the peak I_{Na} densities of these four channel constructs is impeded by the differences in voltage dependence of activation, and no significant differences in peak I_{Na} densities (at −20 or 0 mV) or maximal Na^+ G values (data not shown) were observed for the Na$_V$1.5-S664-671D, compared with WT, channels. Finally, the voltage dependence of steady-state inactivation (Fig. 3 B, Fig. S3 C, and Table 3) and the kinetics of recovery from inactivation (Fig. S3 D and Table 3) of the Na$_V$1.5-S664-671A and Na$_V$1.5-S664-671E quadruple phosphomutant channels were similar to those of the WT channels. Additionally, and to our surprise, no differences in current densities, in the kinetics or voltage dependences of current activation and inactivation, or in the kinetics of recovery from inactivation were observed for

Table 1. **Proteins identified in immunoprecipitated Na_V channel complexes from sham and TAC mouse left ventricles using MS**

Protein	UniProt accession number	No. of exclusive unique peptides	Percentage amino acid sequence coverage	TAC/sham ratio	Protein	UniProt accession number	No. of exclusive unique peptides	Percentage amino acid sequence coverage	TAC/sham ratio
$Na_V1.5$ (Q1080)	K3W4N7	310	56%	1.0	N-cadherin	P15116	13	24%	0.8
$Na_V1.5$ (Q1080del)	Q9JJV9								
$Na_V1.4$	G3X8T7	86	40%	0.8	Plakophilin-2	Q9CQ73	13	20%	0.7
$Na_V1.3$	A2ASI5	24	17%	0.9	Plakophilin-1	P97350	5	8%	0.8
$Na_V1.8$	Q6QIY3	13	9%	0.9	Telethonin	O70548	5	44%	0.8
$Na_V1.7$	Q62205	3	2%	0.7	Desmoglein-2	O55111	13	19%	0.7
$Na_V1.9$	Q9R053	1	1%	1.2	Flotillin-1	O08917	22	59%	0.9
$Na_V1.1$	A2APX8	1	0.5%	1.3	Flotillin-2	Q60634	21	54%	0.8
$Na_V1.2$	B1AWN6	1	0.5%	1.2	14-3-3 zeta/delta	P63101	5	27%	0.9
$Na_V1.6$	F6U329	1	0.6%	1.0	14-3-3 epsilon	P62259	3	17%	1.0
$Na_V\beta4$	Q7M729	11	44%	0.7	14-3-3 gamma	P61982	3	14%	1.0
$Na_V\beta1$	P97952	9	41%	1.0	14-3-3 beta/alpha	Q9CQV8	1	6%	1.1
$Na_V\beta2$	Q56A07	6	37%	0.8	14-3-3 sigma	O70456	1	3%	0.9
Calmodulin	Q3UKW2	12	53%	0.8	Slmap	Q3URD3	1	1%	1.1
FHF2-VY	P70377	37	84%	0.8	αB-Crystallin	P23927	14	71%	0.7
FHF4	P70379	1	7%	0.7	Cx43	P23242	15	50%	0.7
Ankyrin-G	G5E8K5	47	32%	1.0	Kir2.1	P35561	3	11%	0.8
Ankyrin-R	Q02357	2	2%	1.0	CaMKIIγ	Q923T9	11	26%	0.8
Ankyrin-B	S4R245	1	0.4%	0.8	CaMKIIδ	E9Q1T1	2	6%	1.1
Dystrophin	P11531	88	29%	0.9	CaMKIIα	P11798	2	4%	0.8
α1-Syntrophin	A2AKD7	20	53%	0.8	CaMKIIβ	Q5SVI2	1	3%	0.9
β2-Syntrophin	Q61235	19	35%	0.9	PKA, catalytic subunit, α	P05132	2	9%	1.0
α-Actinin-2	Q9JI91	50	60%	0.5	PKAβ-2	Q6PAM0	1	4%	1.1
Caveolin-1	P49817	6	39%	0.8	PKCβ	P68404	2	3%	1.6
Caveolin-2	Q9WVC3	3	28%	0.9	Fyn	P39688	1	2%	1.1
Caveolin-3	P51637	2	11%	0.8	PP2A-C	P63330	1	3%	1.1
Vinculin	Q64727	25	29%	0.7					

The numbers of exclusive unique peptides, the percentage amino acid sequence coverages, and the fold change abundance ratios in TAC left ventricle (n = 5) versus sham left ventricle (n = 4) mαNa_VPAN-IPs for each identified protein are presented. No significant differences in protein abundance were observed between TAC and sham IPs. Cx, connexin; FHF, fibroblast growth factor homologous factor; Kir, inward rectifier K^+ channel; PP2A-C, catalytic subunit of protein phosphatase 2A; Slmap, sarcolemmal membrane-associated protein.

any of the six other heterologously expressed (in HEK-293 cells) paired phosphosilent or phosphomimetic $Na_V1.5$ channels (Fig. S3 and Table 3). Taken together, therefore, these analyses suggest a key role for phosphorylation at S664-671 in regulating the voltage dependence of $Na_V1.5$ channel activation and peak I_{Na} density, whereas the functional impact of the other phosphorylation sites most likely involves more complex mechanisms.

The S664 and S667 phosphorylation sites regulate the voltage dependence of current activation, whereas S671 regulates the peak I_{Na} density

To decipher the respective contributions of the S664, S667, T670, and S671 phosphorylation sites in regulating the voltage dependence of current activation and peak I_{Na} density, each of these serine/threonine residues was mutated individually to alanine or glutamate, and the densities and properties of I_{Na}

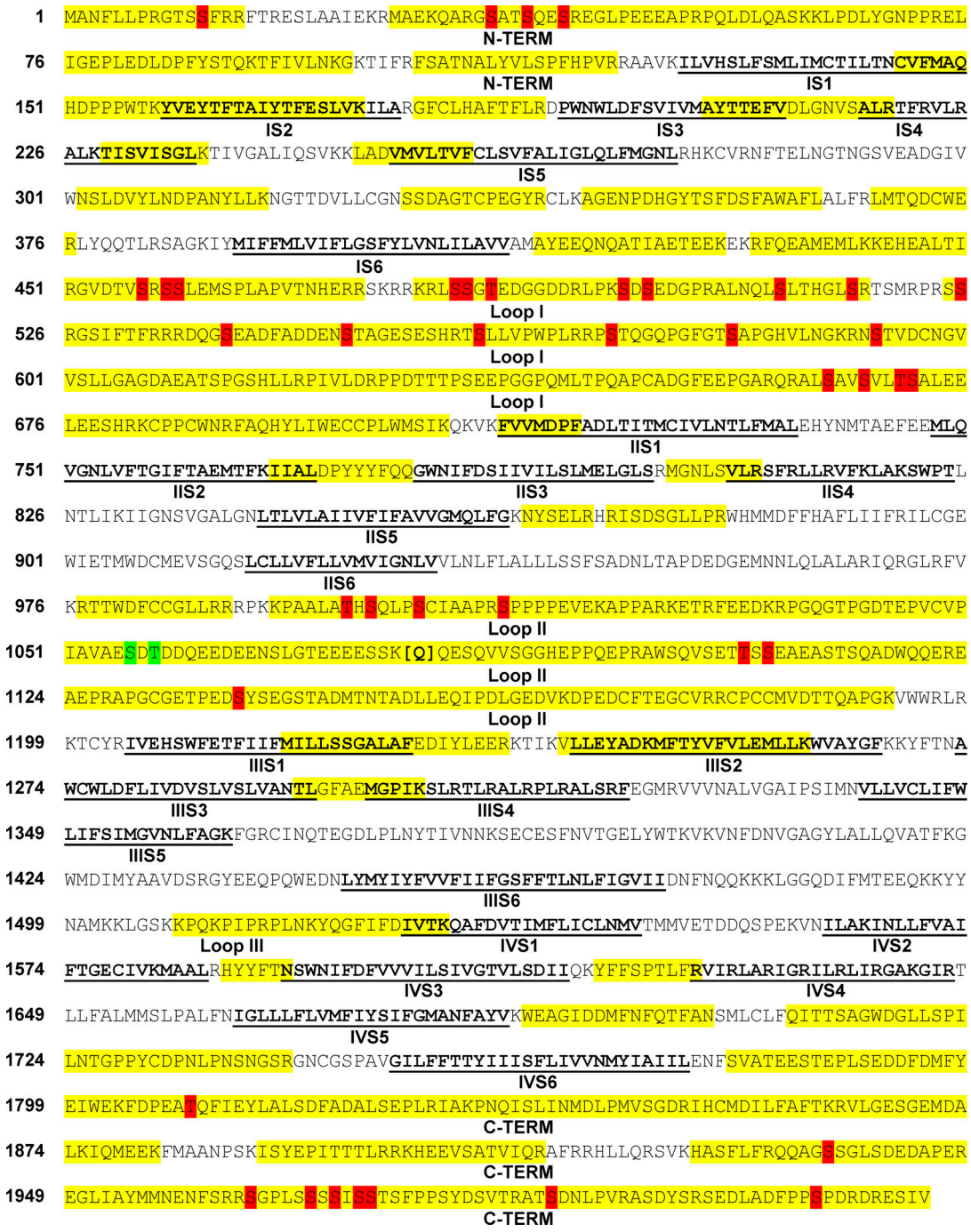

Figure 2. **$Na_V1.5$ amino acid sequence coverage and localization of 42 $Na_V1.5$ phosphorylation sites in mαNa_VPAN-IPs from sham and TAC mouse left ventricles.** Covered sequence and MS-identified phosphorylation sites are highlighted in yellow and red, respectively; transmembrane segments (S1-S6) in each domain (I–IV) are in bold and underlined in black; and loops I, II, and III correspond to interdomains I–II, II–III, and III–IV, respectively. The identification of peptides differing by the presence or absence of a glutamine (Q) at position 1080 ascertains the expression of two $Na_V1.5$ variants: the Q1080 variant corresponds to UniProt reference sequence K3W4N7, and the Q1080del variant corresponds to UniProt reference sequence Q9JJV9. Two phosphorylation site locations are possible at amino acids S1056-T1058 (in green). C-TERM, C terminus; N-TERM, N terminus.

produced by the single phosphosilent or phosphomimetic channel mutants, coexpressed transiently with the accessory $Na_V\beta1$ subunit in HEK-293 cells, were determined. These analyses showed that the voltage dependences of activation of the $Na_V1.5$-S664 (Fig. 4 A) and $Na_V1.5$-S667 (Fig. 4 B) phosphomutant channels are significantly ($P < 0.001$) shifted toward depolarized potentials compared with the WT channels, whereas no changes were observed with the $Na_V1.5$-T670 or $Na_V1.5$-S671 phosphomutant channels (Fig. 4, C and D; see detailed properties and statistics in Table 4). Of note, the ∼6-mV shifts observed with the $Na_V1.5$-S664A and $Na_V1.5$-S667A single phosphosilent channels were twofold smaller than the ∼10-mV shift obtained

Table 2. **Phosphorylation sites, phosphopeptides, and site-discriminating ions identified in immunoprecipitated $Na_V1.5$ proteins from sham and TAC mouse left ventricles using MS**

Phosphorylation site(s)	Phosphopeptide sequence	*m/z* (charge)	−10lgP score	b Ion	Phospho b ion	y Ion	Phospho y ion	TAC/sham ratio
S12	9-GTS(pS)FRR	560.279 (+2)	21.6	b3 (+1)	(-)	y3	(-)	1.2 (*n* = 1)
S36	35-G(pS)ATSQESR	616.279 (+2)	32.1	b1	(-)	y7	(-)	1.3 (*n* = 1)
S42	35-GSATSQE(pS)REGLPEEEAPRPQLDLQASK	887.947 (+4)	73.1	b7 (+1)	(-)	y19 (+2)	y21 (+2)	1.5 ± 0.03 (*n* = 3)
S39 + S42	35-GSAT(pS)QE(pS)REGLPEEEAPRPQLDLQASK	907.937 (+4)	68.4	b4 (+1)	(-)	y19 (+2)	y21	1.2 ± 0.12 (*n* = 2)
S457 (+ S459 or S460)	452-GVDTV(pS)RSSLEMSPLAPVTNHER	957.782 (+3)	77.1	b5 (+1)	b7 (−98) (+2)	y14 (+1)	(-)	1.1 ± 0.09 (*n* = 10)
S459 + S460	452-GVDTVSR(pS)(pS)LEMSPLAPVTNHER	958.117 (+3)	41.5	b7 (+2)	b11 (+2)	y12 (+1)	(-)	1.2 (*n* = 1)
S460	459-S(pS)LEMSPLAPVTNHER	1039.003 (+2)	61.2	b1 (+1)	b4 (+1)	y14 (+1)	(-)	1.0 ± 0.05 (*n* = 18)
S483	481-RL(pS)SGTEDGGDDRLPK	561.038 (+4)	52.4	b2	b3	y13 (+2)	(-)	1.0 ± 0.03 (*n* = 10)
S484	482-LS(pS)GTEDGGDDR	759.319 (+2)	45.7	b2	(-)	y9 (+1)	(-)	1.2 ± 0.07 (*n* = 12)
T486	484-SG(pT)EDGGDDRLPK	628.973 (+3)	21.9	b1	b5	y8 (+2)	(-)	1.2 (*n* = 1)
S483 + S484	480-KRL(pS)(pS)GTEDGGDDRLPK	536.476 (+5)	63	b3	(-)	y12 (+2)	(-)	1.3 ± 0.04 (*n* = 19)
S497	482-LSSGTEDGGDDRLPK(pS)DSEDGPR	732.845 (+4)	60.2	b12 (+2)	(-)	y7 (+1)	y12	1.3 ± 0.07 (*n* = 7)
S483 + S497	481-RL(pS)SGTEDGGDDRLPK(pS)DSEDGPR	791.862 (+4)	40.1	b2	b3 (−98)	y6 (+1)	y12 (+2)	0.7 (*n* = 1)
S484 + S497	482-LS(pS)GTEDGGDDRLPK(pS)DSEDGPR	1003.448 (+3)	54.8	b2 (+1)	b3	y7 (+1)	y12 (+2)	1.7 ± 0.04 (*n* = 2)
S499	497-SD(pS)EDGPR	586.245 (+2)	42	b2	b5	y4 (+1)	y6	1.4 ± 0.17 (*n* = 3)
S510	505-ALNQL(pS)LTHGLSR	573.643 (+3)	51.8	b4 (+1)	(-)	y7 (+1)	(-)	0.9 ± 0.03 (*n* = 3)
S516	505-ALNQLSLTHGL(pS)R	573.644 (+3)	46.7	b9	(-)	y1 (+1)	(-)	0.9 (*n* = 1)
S525	524-S(pS)RGSIFTFR	489.584 (+3)	40.7	b1 (+1)	(-)	y8 (+2)	(-)	0.8 ± 0.09 (*n* = 3)

Table 2. **Phosphorylation sites, phosphopeptides, and site-discriminating ions identified in immunoprecipitated $Na_V1.5$ proteins from sham and TAC mouse left ventricles using MS (*Continued*)**

Phosphorylation site(s)	Phosphopeptide sequence	*m/z* (charge)	−10lgP score	b Ion	Phospho b ion	y Ion	Phospho y ion	TAC/sham ratio
S539	536-DQG(pS)EADFADDENSTAGESESHR	921.701 (+3)	70.9	b3 (+1)	b5 (+1)	y14 (+1)	(-)	1.5 ± 0.09 (*n* = 9)
S549	534-RRDQGSEADFADDEN(pS)TAGESESHR	769.579 (+4)	55.3	b15 (+2)	(-)	y9 (+1)	(-)	3.2 (*n* = 1)
S560	559-T(pS)LLVPWPLR	745.921 (+2)	30.2	b1	b4	y8 (+1)	(-)	1.0 (*n* = 1)
S571	569-RP(pS)TQGQPGFGTSAPGHVLNGK	911.466 (+3)	55.2	b1 (+1)	b7 (+1), b7 (+2)	y19	(-)	0.8 ± 0.03 (*n* = 19)
S581	569-RPSTQGQPGFGT(pS)APGHVLNGK	683.856 (+4)	48.5	b12 (+2)	(-)	y8 (+2)	(-)	0.9 (*n* = 1)
S593	591-RN(pS)TVDCNGVVSLLGAGDAEATSPGSHLLR	841.660 (+4)	71.7	b2	b3	y16 (+1)	(-)	0.8 ± 0.05 (*n* = 4)
S664	662-AL(pS)AVSVLTSALEELEESHRK	936.506 (+3)	60.6	b2 (+1)	b5 (+1)	y18 (+2)	(-)	1.0 ± 0.04 (*n* = 28)
S667	662-ALSAV(pS)VLTSALEELEESHR	817.416 (+3)	64.1	b5 (+1)	b7 (+1)	y13 (+1)	(-)	0.9 ± 0.06 (*n* = 12)
T670	662-ALSAVSVL(pT)SALEELEESHRK	702.629 (+4)	54.3	b7 (+1)	(-)	y12 (+2)	(-)	1.1 ± 0.1 (*n* = 4)
S671	662-ALSAVSVLT(pS)ALEELEESHRK	702.629 (+4)	63.2	b9 (+2)	b10 (+2)	y11 (+2)	(-)	1.7 ± 0.17 (*n* = 12)***
S664 + S667	662-AL(pS)AV(pS)VLTSALEELEESHRK	886.771 (+3)	58.8	b2	b3	y15 (+2)	y18	1.1 ± 0.05 (*n* = 18)
S664 + T670	662-AL(pS)AVSVL(pT)SALEELEESHR	844.072 (+3)	59.3	b2 (+1)	b5 (+1), b8 (+1)	y11 (+1)	(-)	1.0 ± 0.14 (*n* = 3)
S664 + S671	662-AL(pS)AVSVLT(pS)ALEELEESHR	844.072 (+3)	58.3	b2 (+1)	b5 (+1), b9 (+2)	y10 (+1)	(-)	1.8 ± 0.13 (*n* = 9) ***
S667 + T670	662-ALSAV(pS)VL(pT)SALEELEESHRK	722.621 (+4)	54.1	b5 (+1)	b8	y12 (+2)	(-)	1.2 ± 0.37 (*n* = 4)
S667 + S671	662-ALSAV(pS)VLT(pS)ALEELEESHR	844.073 (+3)	60.5	b5 (+1)	b8 (+1), b9	y10 (+1)	(-)	1.4 ± 0.17 (*n* = 7) **
T999	993-KPAALA(pT)HSQLPSCIAAPR	824.114 (+3)	48.8	b6 (+1)	(-)	y12 (+1)	(-)	0.8 (*n* = 1)
S1001	1001-(pS)QLPSCIAAPR	503.591 (+3)	32.6	(-)	b2 (+1)	y8 (+1)	(-)	1.0 ± 0.11 (*n* = 4)

Table 2. **Phosphorylation sites, phosphopeptides, and site-discriminating ions identified in immunoprecipitated $Na_V1.5$ proteins from sham and TAC mouse left ventricles using MS (*Continued*)**

Phosphorylation site(s)	Phosphopeptide sequence	*m/z* (charge)	−10lgP score	b Ion	Phospho b ion	y Ion	Phospho y ion	TAC/sham ratio
S1005	993-KPAALATHSQLP(pS)CIAAPRSPPPPEVEKAPPAR	702.389 (+6)	71.4	b11 (+2)	(-)	y18 (+2)	y21 (+2)	0.8 ± 0.16 (*n* = 2)
S1012	1012-(pS)PPPPEVEK	759.405 (+2)	42.3	(-)	b1 (+1)	y8 (+1)	(-)	0.9 ± 0.03 (*n* = 17)
S1056 and/or T1058	1030-FEEDKRPGQGTPGDTEPVCVPIAVAESDTDDQEEDEENSLGTEEEESSK (1 Phospho)	1230.559 (+5)	57.3	b24 (+2)	(-)	y11 (+1)	(-)	1.8 ± 0.04 (*n* = 5)
T1105	1097-AWSQVSET(pT)SSEAEASTSQADWQQER	1070.132 (+3)	64.3	b8 (+1)	b9	y12 (+1)	(-)	1.1 (*n* = 1)
S1107	1097-AWSQVSETTS(pS)EAEASTSQADWQQER	1070.135 (+3)	69.9	b10 (+1)	b15 (+1)	y14 (+1)	(-)	1.2 (*n* = 1)
S1138	1136-ED(pS)YSEGSTADMTNTADLLEQIPDLGEDVKDPEDCFTEGCVR	1312.582 (+4)	44.7	(-)	b3 (+1)	y23 (+2)	(-)	1.3 ± 0.01 (*n* = 2)
T1809	1809-(pT)QFIEYLALSDFADALSEPLR	903.451 (+3)	54.8	(-)	b1, b2 (+1)	y14 (+1)	(-)	0.8 (*n* = 1)
S1937	1933-QQAG(pS)SGLSDEDAPER	978.430 (+2)	60.1	b4 (+1)	(-)	y11 (+1)	(-)	1.3 (*n* = 1)
S1964	1964-(pS)GPLSSSSISSTSFPPSYDSVTR	885.752 (+3)	50.3	(-)	b1 (+1), b4 (+1)	y14 (+1)	(-)	1.2 ± 0.11 (*n* = 3)
S1969	1964-SGPLS(pS)SSISSTSFPPSYDSVTR	885.753 (+3)	56.9	b5	b6 (+2)	y14 (+1)	(-)	1.0 ± 0.04 (*n* = 3)
S1971	1963-RSGPLSSS(pS)ISSTSFPPSYDSVTR	937.787 (+3)	48.5	b8 (+1)	(-)	y14 (+1)	(-)	0.9 ± 0.09 (*n* = 3)
S1973	1964-SGPLSSSSI(pS)STSFPPSYDSVTR	885.750 (+3)	61.8	b9 (+1)	b10 (+2)	y13	(-)	0.9 ± 0.02 (*n* = 6)
S1974	1964-SGPLSSSSIS(pS)TSFPPSYDSVTR	885.750 (+3)	61.8	b10	(-)	y12 (+1)	(-)	0.9 ± 0.03 (*n* = 2)
S1989	1987-AT(pS)DNLPVR	641.324 (+2)	37.7	b2	b5	y6 (+1)	(-)	0.8 ± 0.07 (*n* = 2)
S2011	2002-SEDLADFPP(pS)PDRDR	675.975 (+3)	38.8	b7 (+1)	(-)	y5 (+2)	y8	1.0 ± 0.05 (*n* = 15)

The site-discriminating ions observed in MS/MS spectra of each annotated $Na_V1.5$ (UniProt reference sequence K3W4N7) phosphopeptide support the assignment of the indicated phosphorylation site(s). The −10lgP scores attest to the quality of peptide identification. The manually verified charge state of unphosphorylated and phosphorylated site-discriminating b and y ions is reported in parentheses. (-) indicates that the ion was not detected. Mean ± SEM phosphopeptide abundance ratios in TAC left ventricles (n = 5) versus sham left ventricles (n = 4) mαNa_VPAN-IPs were calculated from n phosphopeptide(s). **, P < 0.01; ***, P < 0.001; Mann-Whitney test. *m/z*, mass-to-charge ratio.

with the $Na_V1.5$-S664-671A quadruple phosphosilent channel, suggesting that the effects at S664 and S667 are additive. Regarding the analysis of the peak I_{Na} densities, only the $Na_V1.5$-S671E phosphomimetic channel showed a significant (P < 0.05) decrease, compared with the WT channel (Fig. 4 H), whereas no significant differences were observed

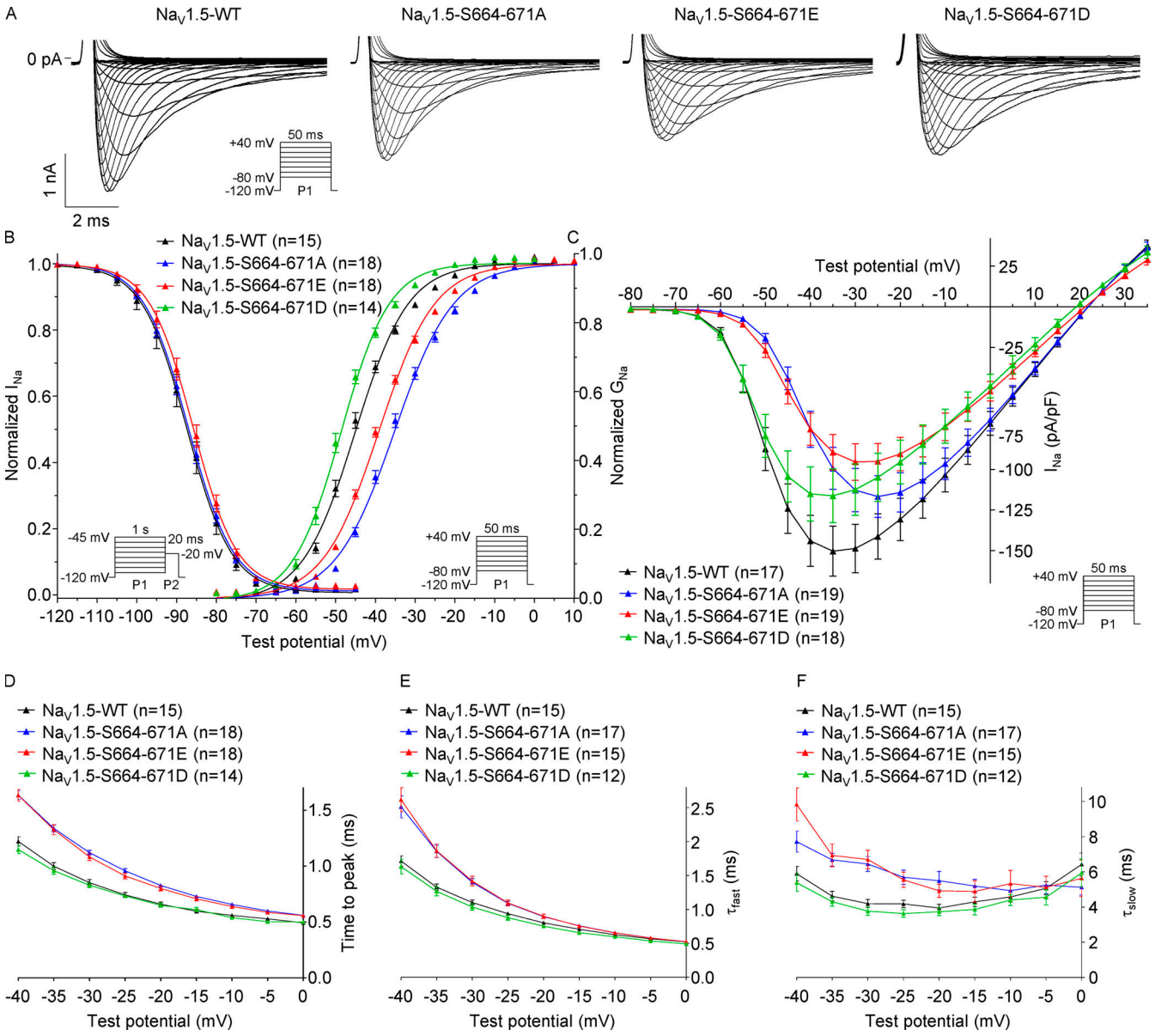

Figure 3. **The phosphorylation sites at positions S664-671 regulate the voltage dependence of current activation and peak I_{Na} density. (A)** Representative whole-cell voltage-gated I_{Na} recorded 48 h following transfection of HEK-293 cells with Na$_V$1.5-WT + Na$_V$β1 (black), Na$_V$1.5-S664-671A + Na$_V$β1 (blue), Na$_V$1.5-S664-671E + Na$_V$β1 (red), or Na$_V$1.5-S664-671D + Na$_V$β1 (green) using the protocols illustrated in each panel. Scale bars are 1 nA and 2 ms. **(B)** Voltage dependences of current activation and steady-state inactivation. The voltage dependence of current activation is shifted toward depolarized potentials in cells expressing the Na$_V$1.5-S664-671A or Na$_V$1.5-S664-671E quadruple phosphomutants compared with cells expressing Na$_V$1.5-WT or the Na$_V$1.5-S664-671D quadruple phosphomimetic channels. **(C)** Mean ± SEM peak I_{Na} densities plotted as a function of test potential. The peak I_{Na} density is reduced in cells expressing the Na$_V$1.5-S664-671E mutant compared with cells expressing Na$_V$1.5-WT. **(D–F)** Mean ± SEM times to peak (D), fast (τ_{fast}; E), and slow (τ_{slow}; F) inactivation time constants plotted as a function of test potential. The times to peak, τ_{fast}, and τ_{slow} are higher in cells expressing the Na$_V$1.5-S664-671A or Na$_V$1.5-S664-671E quadruple phosphomutants than in cells expressing Na$_V$1.5-WT or Na$_V$1.5-S664-671D. Current densities, time- and voltage-dependent properties, and statistical comparisons across groups are provided in Fig. S3 and Table 3. G_{Na}, sodium conductance.

with any of the other single phosphomutant channels (Fig. 4, E–G).

Because phosphorylation at S671 was found to be increased in the TAC, compared with the sham, mαNa$_V$PAN-IPs (Fig. 1 D), and because it was previously suggested that phosphorylation of Na$_V$1.5 may mediate increased I_{NaL} in heart failure (Wagner et al., 2006; Maltsev et al., 2008; Koval et al., 2012; Aiba et al., 2013; Toischer et al., 2013; Glynn et al., 2015), additional voltage-clamp experiments were designed to test whether phosphorylation at S671 regulates I_{NaL}. These analyses showed that none of the single mutations at S671 or quadruple mutations at S664-671 affect TTX-sensitive I_{NaL} density in HEK-293 cells (Fig. S4). Altogether, therefore, these analyses suggest that phosphorylation at S664 and S667 shifts the voltage dependence of current activation toward hyperpolarized potentials in a cumulative manner,

Table 3. **Current densities and properties of $Na_V1.5$ channels mutant for the phosphorylation clusters in transiently transfected HEK-293 cells**

	I_{Na} (pA/pF)	Time to peak (ms)	Time course of inactivation			Voltage-dependence of activation		Voltage-dependence of inactivation		Recovery from inactivation
			τ_{fast} (ms)	τ_{slow} (ms)	A_{fast}/A_{slow}	$V_{1/2}$ (mV)	k (mV)	$V_{1/2}$ (mV)	k (mV)	τ_{rec} (ms)
$Na_V1.5$-WT	−130.8 ± 13.1 (25)	0.60 ± 0.01 (19)	0.72 ± 0.02 (18)	3.6 ± 0.2 (18)	15.5 ± 1.0 (18)	−45.7 ± 0.6 (19)	6.8 ± 0.2 (19)	−88.3 ± 0.6 (19)	4.9 ± 0.1 (19)	8.7 ± 0.6 (19)
$Na_V1.5$-S36-42A	−115.7 ± 11.2 (35)	0.63 ± 0.02 (19)	0.75 ± 0.02 (19)	3.6 ± 0.2 (19)	13.3 ± 1.0 (19)	−44.7 ± 0.6 (19)	6.7 ± 0.1 (19)	−86.5 ± 0.8 (19)	4.9 ± 0.1 (19)	7.1 ± 0.6 (18)
$Na_V1.5$-S36-42E	−92.2 ± 11.4 (31)	0.59 ± 0.02 (19)	0.72 ± 0.02 (17)	3.5 ± 0.2 (17)	13.6 ± 1.9 (17)	−45.2 ± 0.6 (19)	6.6 ± 0.1 (19)	−86.1 ± 0.5 (19)	4.6 ± 0.1 (19)	7.3 ± 0.3 (18)
$Na_V1.5$-S457-460A	−136.5 ± 12.1 (24)	0.60 ± 0.01 (18)	0.75 ± 0.02 (18)	4.6 ± 0.4 (18)	15.6 ± 1.2 (18)	−45.4 ± 0.7 (18)	7.0 ± 0.2 (18)	−90.0 ± 0.9 (18)	5.2 ± 0.1 (18)	9.3 ± 0.5 (18)
$Na_V1.5$-S457-460E	−123.3 ± 11.6 (28)	0.60 ± 0.02 (20)	0.74 ± 0.02 (19)	3.7 ± 0.2 (19)	17.5 ± 1.8 (19)	−45.2 ± 0.4 (20)	6.8 ± 0.1 (20)	−87.5 ± 0.5 (19)	4.7 ± 0.1 (19)	8.7 ± 0.4 (19)
$Na_V1.5$-S483-486A	−104.7 ± 11.3 (40)	0.61 ± 0.02 (28)	0.61 ± 0.02 (26)	3.2 ± 0.1 (26)	12.7 ± 1.0 (26)	−47.1 ± 0.6 (28)	6.3 ± 0.2 (28)	−89.1 ± 0.7 (28)	5.0 ± 0.1 (28)	7.1 ± 0.5 (26)
$Na_V1.5$-S483-486E	−117.4 ± 10.4 (29)	0.55 ± 0.02 (19)	0.59 ± 0.02 (16)	2.9 ± 0.2 (16)	14.2 ± 1.2 (16)	−48.2 ± 0.6 (19)	6.3 ± 0.2 (19)	−89.6 ± 0.6 (19)	4.8 ± 0.1 (19)	8.2 ± 0.6 (16)
$Na_V1.5$-S497-499A	−110.5 ± 13.5 (25)	0.62 ± 0.02 (16)	0.76 ± 0.03 (12)	4.6 ± 0.4 (12)	18.0 ± 1.4 (12)	−44.6 ± 0.6 (16)	7.1 ± 0.1 (16)	−88.4 ± 0.7 (16)	4.8 ± 0.1 (16)	8.8 ± 0.7 (15)
$Na_V1.5$-S497-499E	−129.5 ± 13.8 (22)	0.56 ± 0.01 (18)	0.70 ± 0.02 (17)	3.8 ± 0.2 (17)	16.7 ± 1.0 (17)	−46.7 ± 0.5 (18)	7.2 ± 0.1 (18)	−90.2 ± 0.7 (18)	4.9 ± 0.1 (18)	9.5 ± 0.6 (18)
$Na_V1.5$-S664-671A	−109.8 ± 11.8 (19)	0.83 ± 0.02*** (18)	0.89 ± 0.02** (17)	5.5 ± 0.5* (17)	18.1 ± 1.2 (17)	−35.1 ± 0.6*** (18)	7.3 ± 0.1 (18)	−87.1 ± 0.6 (18)	5.4 ± 0.1 (18)	8.4 ± 0.4 (18)
$Na_V1.5$-S664-671E	−74.5 ± 10.2# (23)	0.80 ± 0.02*** (18)	0.90 ± 0.03* (15)	4.9 ± 0.4 (15)	18.8 ± 1.9 (15)	−39.1 ± 0.4*** (18)	7.0 ± 0.1 (18)	−86.1 ± 0.8 (18)	5.1 ± 0.1 (18)	7.7 ± 0.6 (16)
$Na_V1.5$-S664-671D	−92.2 ± 13.2 (18)	0.65 ± 0.02 (14)	0.77 ± 0.03 (12)	3.7 ± 0.2 (12)	15.5 ± 1.7 (12)	−48.7 ± 0.6 (14)	5.9 ± 0.2 (14)			
$Na_V1.5$-S1003-1010A	−103.0 ± 8.5 (38)	0.62 ± 0.01 (19)	0.76 ± 0.02 (19)	4.2 ± 0.2 (19)	7.4 ± 0.7 (19)	−45.3 ± 0.5 (19)	6.5 ± 0.2 (19)	−86.6 ± 0.7 (19)	6.0 ± 0.2 (19)	6.7 ± 0.6 (19)
$Na_V1.5$-S1003-1010E	−99.9 ± 11.9 (23)	0.61 ± 0.01 (15)	0.74 ± 0.02 (15)	3.9 ± 0.1 (15)	7.8 ± 0.6 (15)	−45.8 ± 0.8 (15)	6.5 ± 0.2 (15)	−86.2 ± 0.8 (15)	5.6 ± 0.2 (15)	6.4 ± 0.5 (13)
$Na_V1.5$-S1964-1969A	−115.0 ± 7.4 (23)	0.63 ± 0.01 (21)	0.77 ± 0.02 (20)	4.1 ± 0.2 (20)	15.8 ± 0.9 (20)	−44.9 ± 0.5 (21)	6.6 ± 0.2 (21)	−87.6 ± 0.5 (21)	5.1 ± 0.1 (21)	7.8 ± 0.4 (18)
$Na_V1.5$-S1964-1969E	−132.8 ± 18.3 (26)	0.66 ± 0.02 (17)	0.81 ± 0.02 (15)	4.0 ± 0.2 (15)	13.9 ± 0.8 (15)	−44.1 ± 0.6 (17)	7.2 ± 0.2 (17)	−89.3 ± 0.8 (17)	4.9 ± 0.1 (17)	9.3 ± 0.8 (15)

Whole-cell voltage-gated I_{Na} were recorded 48 h following transfection of HEK-293 cells with the WT or the mutant $Na_V1.5$ channels and the $Na_V\beta1$ channel subunit using the protocols described in the Materials and methods section. The peak I_{Na} density, time to peak, and time course of inactivation properties presented were determined from analyses of records obtained on depolarizations to −20 mV (HP = −120 mV). All values are means ± SEMs. The number of cells analyzed is provided in parentheses. #, $P < 0.05$ versus $Na_V1.5$-WT, one-way ANOVA followed by Dunnett's post-hoc test. *, $P < 0.05$; **, $P < 0.01$; ***, $P < 0.001$ versus $Na_V1.5$-WT; Kruskal-Wallis followed by Dunn's post-hoc test.

whereas phosphorylation at S671 decreases the peak I_{Na} density.

The S671 phosphorylation site regulates the cell surface expression of $Na_V1.5$ channels

Additional cell surface biotinylation experiments in transiently transfected HEK-293 cells were designed to determine whether the S671 phosphorylation site regulates the cell surface expression of the $Na_V1.5$ channel protein. Interestingly, these experiments revealed that the cell surface expression of the $Na_V1.5$-S671E phosphomimetic channel is significantly ($P < 0.001$) decreased compared with the WT or the $Na_V1.5$-S671A phosphosilent channels, whereas no differences in total $Na_V1.5$ protein expression were observed (Fig. 5, A and B). Importantly, the decrease observed with the phosphomimetic mutant, compared with the phosphosilent mutant, suggests that not only this channel locus, but also most probably phosphorylation at this particular site, underlie the observed decrease in cell surface expression. Together with the electrophysiological findings, therefore, these biochemical analyses demonstrate a key role for S671 in regulating the cell surface expression of $Na_V1.5$, and suggest that phosphorylation at this site decreases the cell surface expression of $Na_V1.5$-encoded channels.

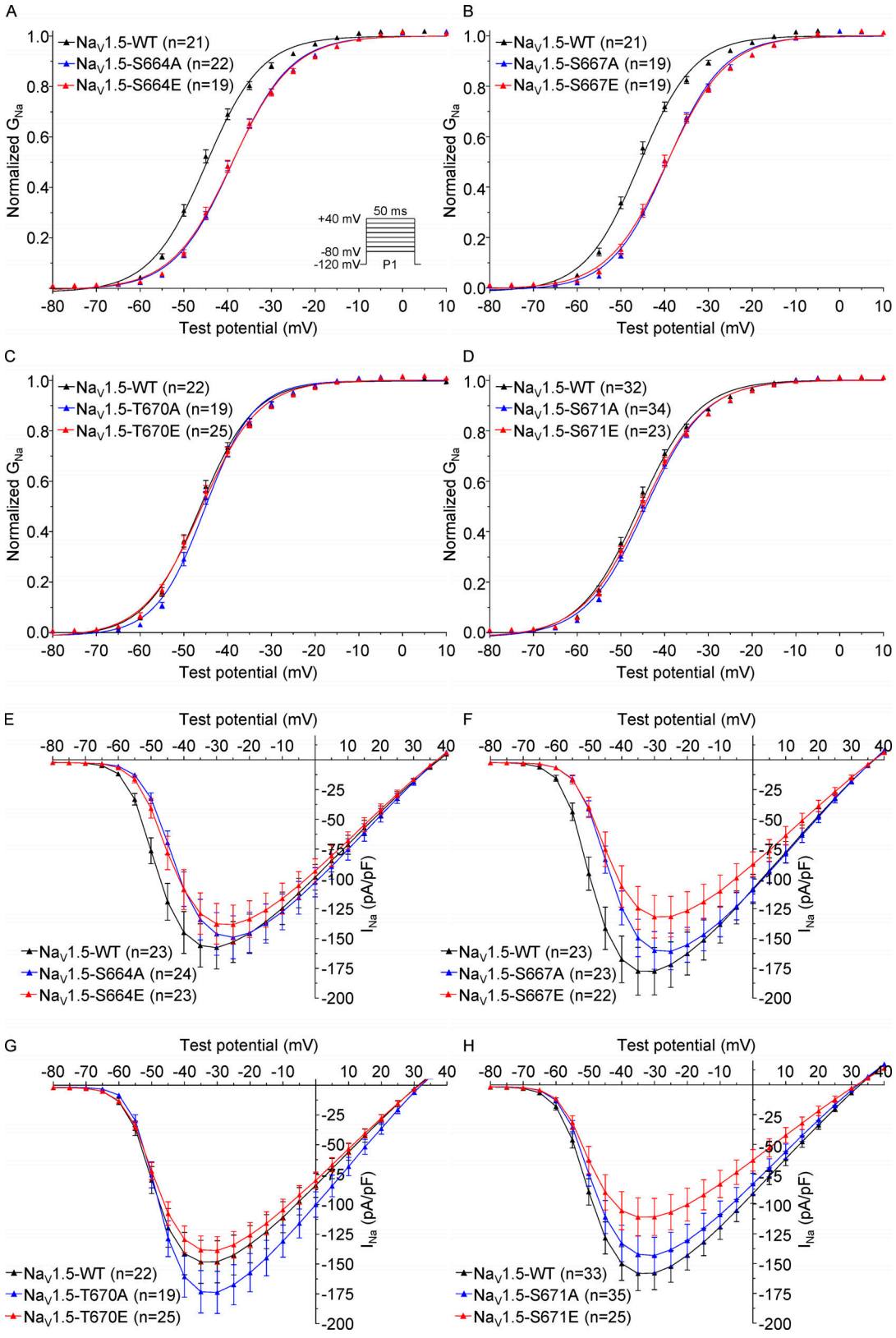

Figure 4. **The S664 and S667 phosphorylation sites regulate the voltage dependence of current activation, whereas the S671 phosphorylation site regulates the peak I_{Na} density.** Currents were recorded as described in the legend to Fig. 3. **(A–D)** The voltage dependence of current activation is shifted toward more depolarized potentials in cells expressing $Na_V1.5$-S664A (A), $Na_V1.5$-S664E (A), $Na_V1.5$-S667A (B), or $Na_V1.5$-S667E (B) than in cells expressing $Na_V1.5$-WT, whereas no significant differences are observed with the $Na_V1.5$-T670 (C) or $Na_V1.5$-S671 (D) phosphomutants. **(E–H)** The mean ± SEM peak I_{Na} densities are plotted as a function of test potential. The peak I_{Na} density is reduced in cells expressing $Na_V1.5$-S671E (H), compared with cells expressing $Na_V1.5$-WT, whereas no significant differences are observed with the other phosphomutants. Current densities, time- and voltage-dependent properties, and statistical comparisons across groups are provided in Table 4. G_{Na}, sodium conductance.

Table 4. **Current densities and properties of $Na_V1.5$ channels mutant for S664, S667, T670, and S671 in transiently transfected HEK-293 cells**

	I_{Na} (pA/pF)	Time to peak (ms)	Time course of inactivation			Voltage dependence of activation		Voltage dependence of inactivation		Recovery from inactivation
			τ_{fast} (ms)	τ_{slow} (ms)	A_{fast}/A_{slow}	$V_{1/2}$ (mV)	k (mV)	$V_{1/2}$ (mV)	k (mV)	τ_{rec} (ms)
$Na_V1.5$-WT	−162.5 ± 18.0 (23)	0.62 ± 0.02 (21)	0.75 ± 0.02 (19)	3.3 ± 0.2 (19)	13.8 ± 1.5 (19)	−45.7 ± 0.6 (21)	6.0 ± 0.2 (21)	−85.0 ± 0.6 (21)	4.7 ± 0.1 (21)	6.0 ± 0.4 (17)
$Na_V1.5$-S664A	−145.2 ± 17.4 (24)	0.75 ± 0.01* (22)	0.82 ± 0.02 (21)	4.1 ± 0.2 (21)	16.7 ± 1.4 (21)	−38.9 ± 0.5*** (22)	6.6 ± 0.1 (22)	−84.0 ± 0.7 (22)	4.8 ± 0.1 (22)	6.6 ± 0.6 (22)
$Na_V1.5$-S664E	−133.6 ± 15.4 (23)	0.73 ± 0.02 (19)	0.79 ± 0.03 (14)	3.3 ± 0.2 (14)	11.7 ± 1.1 (14)	−39.0 ± 0.6*** (19)	6.7 ± 0.1 (19)	−83.4 ± 0.8 (19)	4.7 ± 0.1 (19)	6.1 ± 0.5 (19)
$Na_V1.5$-S667A	−155.3 ± 14.6 (23)	0.75 ± 0.02 (19)	0.78 ± 0.03 (16)	3.9 ± 0.2 (16)	14.1 ± 1.0 (16)	−39.4 ± 0.5*** (19)	6.3 ± 0.2 (19)	−83.7 ± 0.6 (19)	4.9 ± 0.1 (19)	6.0 ± 0.4 (16)
$Na_V1.5$-S667E	−126.7 ± 16.0 (22)	0.76 ± 0.02* (19)	0.81 ± 0.02 (14)	4.0 ± 0.2 (14)	14.9 ± 1.3 (14)	−39.5 ± 0.7*** (19)	6.6 ± 0.1 (19)	−83.8 ± 0.9 (19)	4.7 ± 0.1 (19)	6.7 ± 0.7 (19)
$Na_V1.5$-T670A	−157.2 ± 16.0 (19)	0.63 ± 0.02 (19)	0.64 ± 0.02 (18)	3.0 ± 0.2 (18)	11.2 ± 1.5 (18)	−45.1 ± 0.6 (19)	5.4 ± 0.2 (19)	−86.9 ± 0.9 (16)	4.8 ± 0.1 (16)	8.4 ± 0.6 (14)
$Na_V1.5$-T670E	−125.7 ± 10.5 (25)	0.59 ± 0.02 (25)	0.70 ± 0.02 (22)	3.5 ± 0.4 (22)	14.3 ± 1.9 (22)	−46.2 ± 0.7 (25)	6.3 ± 0.2 (25)	−87.7 ± 1.0 (20)	4.6 ± 0.1 (20)	9.8 ± 1.0 (20)
$Na_V1.5$-S671A	−130.7 ± 13.7 (35)	0.54 ± 0.02 (34)	0.59 ± 0.02 (25)	2.3 ± 0.1 (25)	10.3 ± 0.9 (25)	−44.4 ± 0.5 (34)	6.5 ± 0.1 (34)	−84.9 ± 0.6 (32)	4.5 ± 0.1 (32)	5.6 ± 0.3 (30)
$Na_V1.5$-S671E	−100.6 ± 13.8# (25)	0.52 ± 0.01 (23)	0.65 ± 0.02 (11)	2.7 ± 0.3 (11)	9.9 ± 1.6 (11)	−45.0 ± 0.5 (23)	6.8 ± 0.1 (23)	−86.1 ± 0.5 (23)	4.4 ± 0.1 (23)	6.4 ± 0.3 (21)

Whole-cell voltage-gated I_{Na} were recorded 48 h following transfection of HEK-293 cells with the WT or the mutant $Na_V1.5$ channels and the $Na_V\beta1$ channel subunit using the protocols described in the Materials and methods section. The peak I_{Na} density, time to peak, and time course of inactivation properties presented were determined from analyses of records obtained on depolarizations to −20 mV (HP = −120 mV). All values are means ± SEMs. The number of cells analyzed is provided in parentheses. #, $P < 0.05$ versus $Na_V1.5$-WT, one-way ANOVA followed by Dunnett's post-hoc test. *, $P < 0.05$; ***, $P < 0.001$ versus $Na_V1.5$-WT; Kruskal-Wallis followed by Dunn's post-hoc test.

Simulated consequences of phosphorylation on the first intracellular linker loop of $Na_V1.5$

Like many heavily phosphorylated protein segments (Iakoucheva et al., 2004; Wright and Dyson, 2015), the first two intracellular linker loops of $Na_V1.5$ are predicted to be intrinsically disordered. Conformational heterogeneity is one of the defining hallmarks of intrinsically disordered regions (IDRs). Heterogeneity is manifest in the amplitude of fluctuations of overall size, shape, and local secondary structural preferences. There is growing recognition of sequence specificity whereby the ensembles accessible to an IDR are governed by the amino acid composition, extent of phosphorylation, and patterning of residues within the linear sequence. These sequence–ensemble relationships can be uncovered using all-atom simulations. Given the disparate time scales and length scales involved, a robust and efficient approach is to use Markov chain Metropolis Monte Carlo simulations based on the ABSINTH implicit solvent model as implemented in the CAMPARI simulation (Vitalis and Pappu, 2009b; Mao et al., 2010; Das and Pappu, 2013). Here, we used simulations to quantify sequence–ensemble relationships for the first intracellular linker loop of human $Na_V1.5$ containing the phosphorylation clusters S457-460, S483-486, S497-499, and S664-671 identified by MS. For our simulations, we used segments between 30 and 40 residues in length, containing each cluster in an approximately central position (441-480 for S457-460, 465-501 for S483-486, 481-515 for S497-499, 651-684 for S664-671). For each cluster, we performed simulations for the WT sequence, as well as phosphomimetic mutations where serine(s)/threonine(s) are replaced with glutamate(s). The results of simulations were analyzed using the device of internal scaling plots. These plots quantify the variation of ensemble-averaged distances between residues i and j as a function of sequence separation |j-i|. Multiple pairs of residues contribute to a given sequence separation |j-i|. The internal scaling profiles can be calibrated against reference profiles that pertain to two kinds of random-coil ensembles. These are designated as EV, which pertains to profiles extracted for self-avoiding walks, and FRC, which pertains to profiles extracted for FRCs. Details of these reference ensembles have been published elsewhere.

Simulations of the 441-480 segment showed that the conformational preferences of the unphosphorylated (WT) peptide are akin to those of the FRC reference (Fig. 6 A). This implies that sequence encodes a conformational averaging whereby the peptide–solvent and peptide–peptide interactions are mutually compensatory, thereby giving rise to an ensemble that is maximally heterogeneous. Introduction of phosphomimetic substitutions S457E, S459E, and/or S460E did not have a large effect on the ensemble-averaged internal scaling profiles when compared with the unmodified sequence. We obtained similar results for the 465-501 segment, which is also largely unaffected by the introduction of the phosphomimetic mutation(s) of the S483-486 cluster (Fig. 6 B). Conversely, the 481-515 and 651-684 segments were noticeably sensitive to the addition of

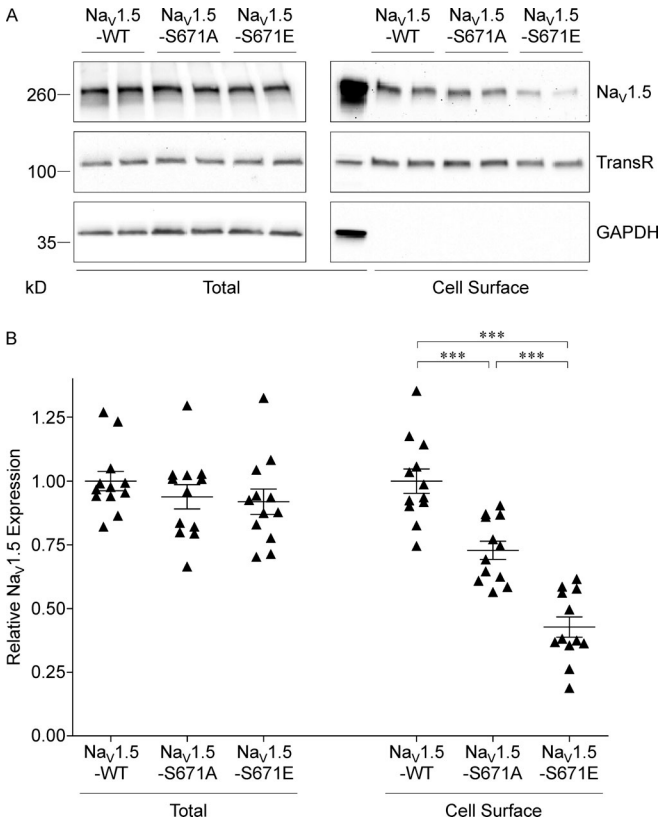

Figure 5. **The S671 phosphorylation site regulates the cell surface expression of $Na_V1.5$. (A)** Representative Western blots of total (left panel) and cell surface (right panel) $Na_V1.5$ from HEK-293 cells transiently transfected with $Na_V1.5$-WT + $Na_V\beta1$, $Na_V1.5$-S671A + $Na_V\beta1$, or $Na_V1.5$-S671E + $Na_V\beta1$. Samples were probed in parallel with the anti–transferrin receptor (TransR) and anti-GAPDH antibodies. **(B)** Mean ± SEM total and cell surface $Na_V1.5$ protein expression in transiently transfected HEK-293 cells (n = 12 in six different experiments). Expression of $Na_V1.5$ in each sample was first normalized to the TransR protein in the same blot and then expressed relative to $Na_V1.5$ protein expression (total or cell surface) in cells transfected with $Na_V1.5$-WT + Navβ1. Relative (mean ± SEM) $Na_V1.5$ cell surface expression is different (***, $P < 0.001$, one-way ANOVA followed by the Dunnett's post-hoc test) in cells expressing $Na_V1.5$-WT, $Na_V1.5$-S671A, and $Na_V1.5$-S671E channels.

the negative charges (Fig. 6, C and D). When unphosphorylated, these segments preferred conformations that are considerably more compact than the FRC reference. Upon the introduction of cumulative phosphomimetic mutations, these segments gradually expanded in the direction of the EV limit.

Taken together, the results suggest that the intrinsic conformational preferences of the WT sequence dictate the extent of responsiveness of the conformational ensemble to multisite phosphorylation. Sequence stretches that have an intrinsic preference for FRC-like conformations are relatively insensitive to phosphomimetic substitutions of serine/threonine residues. This insensitivity has been quantified for IDRs that undergo multisite phosphorylation (Martin et al., 2016). In contrast, sequences that have an intrinsic preference for compact conformations become responsive to phosphomimetic substitutions. This would appear to derive from the increased fraction of charged residues (FCR; which engenders preferential solvation) and electrostatic repulsions (Mao et al., 2010). The FCR and the net charge per residue are known to be direct determinants of the conformational preferences of IDRs (Holehouse and Pappu, 2018). Both the 441-480 and 465-501 segments have a higher FCR than the 481-515 and 651-684 segments. The addition of a single negative charge would lead to a greater percentage increase in the FCR of the 481-515 and 651-684 segments than it would for the 441-480 and 464-501 segments. As the latter are already expanded, additional charges do not have a large impact on the conformational preference. The more compact starting point of the former allows the phosphomimetic mutations to have a greater effect. While the results for three of the clusters were consistent with the experimental data, those for the S497-499 cluster present an apparent inconsistency. These observations suggest that the ability of this segment to expand due to the addition of charge is not connected to channel gating. Together with the electrophysiological analyses, therefore, these simulations suggest that the effect of phosphorylation at S664 and S667 on the voltage dependence of channel activation is mediated by the expansion of the area containing the phosphorylation sites and that this expansion is likely to regulate channel activation allosterically.

Discussion

The results presented here provide a novel, detailed phosphorylation map of the native mouse left ventricular $Na_V1.5$ channel protein, and identify the functional roles of three of these phosphorylation sites in regulating the expression and gating properties of $Na_V1.5$-encoded channels. The highly phosphorylated S664 and S667 regulate the voltage dependence of channel activation in an additive manner, whereas S671, in which phosphorylation is increased in TAC mouse left ventricles, regulates $Na_V1.5$ cell surface expression and peak I_{Na} density. No additional roles could be assigned to the other clusters of $Na_V1.5$ phosphorylation sites, suggesting additional complexity in the mechanisms mediating the phosphorylation-dependent regulation of cardiac $Na_V1.5$ channels.

Phosphorylation map of native mouse left ventricular $Na_V1.5$ channels

The present phosphoproteomic analysis confidently identified a total of 42 native phosphorylation sites in the $Na_V1.5$ channel protein purified from mouse left ventricles, of which 19 are novel (Table S2). 17 of these sites were also found to be phosphorylated in heterologously expressed human $Na_V1.5$ channels (Herren et al., 2015), suggesting that about half of this phosphorylation pattern is conserved among species (mouse and human) and cellular systems (native channels in left ventricles and recombinant channels in HEK-293 cells), whereas the others may be associated with more specific and/or localized regulation. Among the sites identified, only six were previously suggested to be the targets for specific kinases using in silico and/or in vitro analyses: S36 and S525 were attributed to the regulation by PKA; S484 and S664 were assigned to the serum- and glucocorticoid-inducible kinase 3 (SGK3); and S516 and S571 were ascribed to CaMKII (reviewed in Marionneau and Abriel,

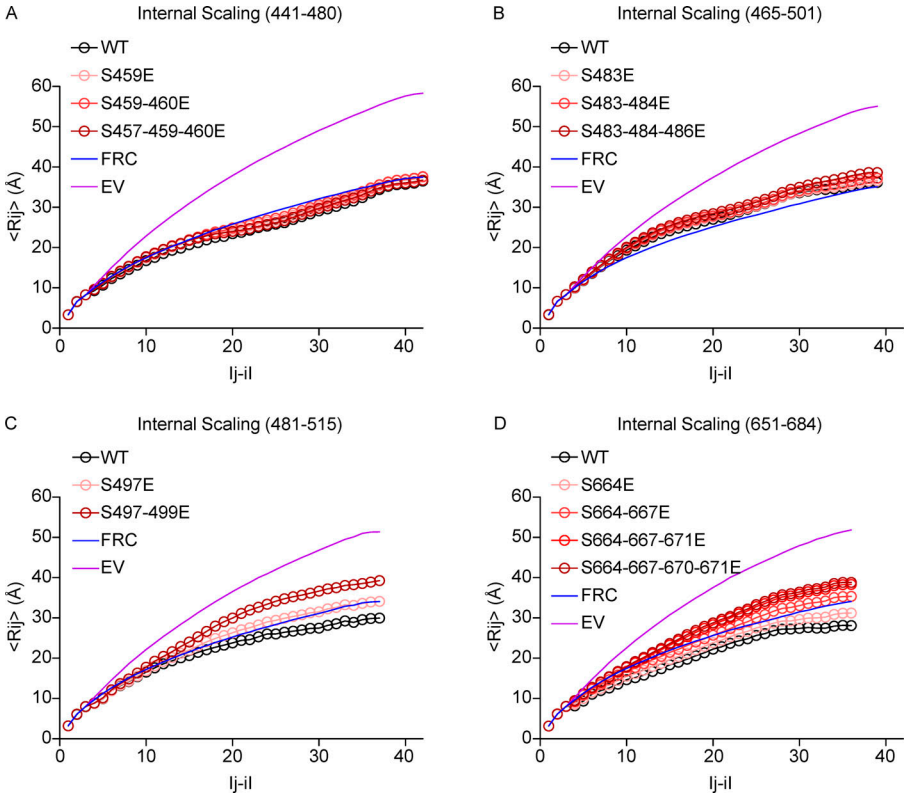

Figure 6. **Simulations of phosphorylation of segments of the first intracellular linker loop of $Na_V1.5$.** The sequential distance between a pair of residues is on the x axis, and the average spatial distance between a pair of residues separated by the specified sequential distance is on the y axis. <Rij> is the average simulated spatial distance between all residue pairs separated in the amino acid sequence by |j-i| residues. The WT sequences are plotted in black. Phosphorylation is simulated by single or multiple replacement of serines/threonines with glutamates (E), and resulting simulations are plotted in gradations of red. The FRC (in blue) and EV (in purple) limits are plotted for reference (see text). **(A)** Sequence 441-480 contains the phosphosites S457, S459, and S460. **(B)** Sequence 465-501 contains the phosphosites S483, S484, and T486. **(C)** Sequence 481-515 contains the phosphosites S497 and S499. **(D)** Sequence 651-684 contains the phosphosites S664, S667, T670, and S671.

2015). In marked contrast, several previously described phosphorylation sites were not detected in the present study, including the PKA-dependent S528, the CaMKII-associated T594, the PKC-dependent S1506, the adenosine monophosphate–activated protein kinase (AMPK)–dependent T101 (Liu et al., 2019), and the six Fyn-dependent tyrosines (Ahern et al., 2005; Iqbal et al., 2018). Although these latter sites have never been identified in native cardiac tissues and may simply not exist in the myocardium, it is also possible that the MS detection of these sites here was prevented because of technical limitations. Indeed, a few cytoplasmic regions of the channel were not covered in our analysis, most probably because of the presence of too many, or on the contrary not enough, surrounding tryptic cleavage sites (see regions not highlighted in Fig. 2). These areas comprise a total of 24 serine/threonine/tyrosine residues, including T101 and S1506, which may, therefore, have been missed. Additionally, the low levels of threonine and tyrosine phosphorylation, compared with phosphoserines, may have limited the identification of phosphothreonines and phosphotyrosines (Johnson and White, 2012). Overall, of the 188 cytoplasmic serine/threonine/tyrosine residues in $Na_V1.5$, 42 (22%) are phosphorylated, and 24 (13%) are not identified in the MS data acquired.

Strikingly, and consistent with previous studies from our laboratory (Marionneau et al., 2012b; Burel et al., 2017) and the Bers group (Herren et al., 2015), the results obtained and presented here again revealed that the first intracellular linker loop of $Na_V1.5$ is a hot spot for phosphorylation, with a total of 21 sites identified. Comparisons of the relative abundances of the phosphopeptides identified three highly abundant (and highly phosphorylated) clusters of phosphorylation sites in the first intracellular linker loop of $Na_V1.5$ in mouse left ventricles. Retrospectively, it is interesting to note that these most abundant phosphorylation sites were already detected in previous less sensitive MS analyses from our laboratory (Marionneau et al., 2012b; Burel et al., 2017; see Table S2). The simplest interpretation of these findings is that these three phosphorylation clusters, at positions S457-S460, S483-T486, and S664-S671, are likely involved in regulating the basal and/or gating properties of native cardiac $Na_V1.5$ channels. Conversely, the other phosphorylation sites, with lower stoichiometries, may play spatially or temporally distinct roles in the physiological or more pathophysiological regulation of channel expression or gating. This suggestion is highlighted for residue S671, for example, which is substantially (10-fold) less phosphorylated than the nearby S664 and S667 residues in WT mouse left ventricles, but is (twofold) up-regulated in TAC left ventricles. Remarkably, this MS analysis also revealed that the vast majority of identified phosphorylation sites (at least 26) are clustered, suggesting concomitant phosphorylation and roles in regulating channel expression and/or function. Unexpectedly, however, except for S664, S667, and S671, no apparent effects of phosphomimetic or phosphosilent mutations were observed on heterologously expressed (in HEK-293 cells) $Na_V1.5$ current densities or biophysical properties, suggesting a greater complexity than anticipated in the mechanisms contributing to phosphorylation-dependent regulation of $Na_V1.5$ channels.

The S664 and S667 phosphorylation sites regulate the voltage dependence of $Na_V1.5$ channel activation

The electrophysiological analyses presented here identified key roles of S664 and S667 in regulating the voltage dependence of $Na_V1.5$ channel activation. Indeed, the data demonstrate that the voltage dependence of activation of the quadruple phosphosilent channels at positions S664-671 is shifted toward depolarized potentials, compared with the WT and the quadruple aspartate phosphomimetic channels, whereas the quadruple glutamate phosphomimetic channels display a smaller shift. These findings are consistent with WT channels being phosphorylated at S664 and S667 in HEK-293 cells, as previously reported (Herren et al., 2015), and suggest that disruption of phosphorylation at these sites impacts channel gating.

Further analyses of the roles of each of the four phosphorylation sites in this cluster revealed the specific involvement of S664 and S667 in regulating gating, whereas modifying T670 or S671 was without effects. Interestingly, however, the single glutamate mutations at S664 and S667 produced the same effects as the single phosphosilent mutations. These observations suggest that the consequences of glutamate substitution, which introduces a single negative charge with a small hydrated shell, and the addition of a phosphate group, which introduces two negative charges with a large hydrated shell (Hunter, 2012), are functionally quite distinct. It also seems likely that one glutamate at these loci (in single S664 and S667 phosphomimetic channels) is not sufficient to mimic phosphorylation and that multiple glutamates (i.e., in the quadruple phosphomimetic channel) only partially mimic phosphorylation. The fact that the shifts induced by the single phosphosilent mutations are half the shift generated by the quadruple phosphosilent mutation further supports this hypothesis and suggests that regulation involving these two sites is cumulative and most likely concomitant. Nevertheless, further investigations, aimed at demonstrating the role of phosphorylation, rather than any other structural determinants associated with this locus, are certainly warranted. In this regard, our findings are also in accordance with previous data reporting the role of SGK3 in shifting the voltage dependence of channel activation toward more hyperpolarized potentials in *Xenopus laevis* oocytes, whereas the opposite effect was observed with the $Na_V1.5$-S664A phosphosilent channel (Boehmer et al., 2003). Although the involvement of SGK3 and S664 in a shared regulation was not directly shown in this previous study, it is tempting to speculate that SGK3 may constitute the kinase phosphorylating S664 and S667 and mediating this regulation.

The effects of phosphorylation were also analyzed using an all-atom simulations approach to determine how the introduction of negative charges affects the conformational ensemble of the segments containing the phosphorylation clusters identified by MS. These simulations demonstrate that the introduction of negative charges at positions S497-S499 and S664-671 could expand the structure of the containing segments, whereas no effects are likely with the segments containing the S457-460 and S483-486 phosphorylation clusters. Furthermore, for both of the affected segments, the expansion likely gradually increases with the cumulative addition of charges. Interestingly, the simulation findings are consistent with the additive roles of S664 and S667 in regulating the voltage dependence of channel activation observed in the electrophysiological analyses. Consistent with the proximity of the S664-671 phosphorylation cluster to the DII voltage-sensing domain of $Na_V1.5$, which is tightly linked to channel activation (Varga et al., 2015), our findings suggest that phosphorylation at S664 and S667 regulates channel activation through the expansion of the C-terminal extremity of the first intracellular linker loop of the channel. However, no effects on channel gating were observed with the S497-499 phosphomimetic mutant, even though the simulation showed an effect on its ability to expand. This result suggests that the expansion of this segment, which is more distal to the DII voltage-sensing domain, does not regulate channel gating.

The S671 phosphorylation site regulates $Na_V1.5$ channel cell surface expression and peak I_{Na} density

The functional analyses also demonstrate that mimicking phosphorylation at S671 decreases the expression of the $Na_V1.5$ protein at the cell surface, as well as peak I_{Na} density in HEK-293 cells. These results suggest that S671 is not phosphorylated in HEK-293 cells, which is in agreement with the previously published MS analyses (Herren et al., 2015). While the phosphomimetic mutation greatly decreases the cell surface expression of $Na_V1.5$, the phosphosilent mutation also reduces $Na_V1.5$ surface expression, albeit to a much smaller extent. These confounding results suggest that the regulation mediated by this locus highly depends on structural changes and that the phosphomimetic mutation affects the cell surface expression of the channel in part through a change in the structure of the locus. One could further suggest that the greater effect of the phosphomimetic channel may be caused by additional attributes common to the phosphate group and the glutamate side chain. Together, therefore, these findings highlight the novel role of this locus, and potentially of phosphorylation at this site, in regulating the cell surface expression of $Na_V1.5$ channels.

Interestingly, the MS analyses also revealed that phosphorylation at S671 is increased in the left ventricles of TAC mice, suggesting a role in mediating the Na_V channel defects associated with heart failure. Because previous studies have suggested that CaMKII-dependent phosphorylation of $Na_V1.5$ may constitute one of the molecular mechanisms mediating the increased I_{NaL} in heart failure (Wagner et al., 2006; Maltsev et al., 2008; Koval et al., 2012; Aiba et al., 2013; Toischer et al., 2013; Glynn et al., 2015), this finding prompted us to examine the I_{NaL} generated by the phosphosilent and phosphomimetic $Na_V1.5$ mutants at position 671. Our results herein appeared negative, although it cannot be excluded that this regulation may require a specific molecular and cellular environment that is not recapitulated in HEK-293 cells. Additionally, and to our surprise, no changes in phosphorylation at S571 were observed in our TAC model, in contrast with previous findings in nonischemic human heart failure (Koval et al., 2012) and in several animal models of heart disease (Koval et al., 2012; Toischer et al., 2013; Glynn et al., 2015). These seemingly disparate findings may reflect technical and/or experimental differences, including differences in the models used and/or stages of disease.

The results presented here raise the interesting and novel possibility that increased phosphorylation at S671 participates in decreasing the peak I_{Na} often observed in heart failure. Consistent with this suggestion, a recent study by the Remme group, using superresolution microscopy, showed a reduction in the size of $Na_V1.5$ clusters in TAC ventricular myocytes without any changes in $Na_V1.5$ transcript or total protein expression (Rivaud et al., 2017). Although further studies will be required to determine directly whether these observations are causally linked to increased phosphorylation at S671, the results here provide new hints at understanding the molecular basis of the decreased peak I_{Na} in heart failure.

Altogether, the results presented here demonstrate that native mouse ventricular $Na_V1.5$ is highly phosphorylated and that the mechanisms mediating the phosphorylation-dependent regulation of $Na_V1.5$-encoded channels are site-specific, complex, and dynamic and lead to diverse physiological and/or pathological consequences on both channel gating and expression.

Acknowledgments

Olaf S. Andersen served as editor.

The expert technical assistance of Petra Erdmann-Gilmore, Yiling Mi, and Rose Connors is gratefully acknowledged.

This work was supported by the Agence Nationale de la Recherche (ANR-15-CE14-0006-01 and ANR-16-CE92-0013-01 to C. Marionneau), the Deutsche Forschungsgemeinschaft (Ma 1982/5-1 to L.S. Maier), and the National Institutes of Health (R01-HL148803 to C. Marionneau, R.V. Pappu, and J.R. Silva; R01-HL034161 and R01-HL142520 to J.M. Nerbonne; and 5R01NS056114 to R.V. Pappu). The MS experiments were performed at the Washington University Proteomics Shared Resource (WU-PSR), which is supported in part by the WU Institute of Clinical and Translational Sciences (National Center for Advancing Translational Sciences grant UL1 TR000448), the Mass Spectrometry Research Resource (National Institute of General Medical Sciences grant P41 GM103422), and the Siteman Comprehensive Cancer Center Support Grant (National Cancer Institute grant P30 CA091842). M. Lorenzini was supported by a Groupe de Réflexion sur la Recherche Cardiovasculaire–Société Française de Cardiologie predoctoral fellowship (SFC/GRRC2018). S. Burel was supported by a Fondation Lefoulon Delalande postdoctoral fellowship. The content of the research reported is solely the responsibility of the authors and does not necessarily represent the official views of the funding agencies.

The authors declare no competing financial interests.

Author contributions: C. Marionneau designed the study and wrote the paper. C. Marionneau, D. Maloney, J.M. Nerbonne, R.R. Townsend, and L.S. Maier designed, performed, and/or analyzed the MS experiments. M. Lorenzini, S. Burel, A. Lesage, C. Charrière, P.-M. Chevillard, B. Evrard, J.M. Nerbonne, and C. Marionneau designed, performed, and/or analyzed the functional analyses. E. Wagner, K.M. Ruff, R.V. Pappu, and J.R. Silva designed, performed, and/or analyzed the modeling analyses. S. Wagner and L.S. Maier provided the sham/TAC mice and performed mouse echocardiography. All authors reviewed the results and approved the final version of the manuscript.

Submitted: 2 May 2020
Revised: 23 October 2020
Accepted: 3 December 2020

References

Ahern, C.A., J.F. Zhang, M.J. Wookalis, and R. Horn. 2005. Modulation of the cardiac sodium channel NaV1.5 by Fyn, a Src family tyrosine kinase. *Circ. Res.* 96:991–998. https://doi.org/10.1161/01.RES.0000166324.00524.dd

Aiba, T., A.S. Barth, G.G. Hesketh, Y.L. Hashambhoy, K. Chakir, R.S. Tunin, J.L. Greenstein, R.L. Winslow, D.A. Kass, and G.F. Tomaselli. 2013. Cardiac resynchronization therapy improves altered Na channel gating in canine model of dyssynchronous heart failure. *Circ. Arrhythm. Electrophysiol.* 6:546–554. https://doi.org/10.1161/CIRCEP.113.000400

Ashpole, N.M., A.W. Herren, K.S. Ginsburg, J.D. Brogan, D.E. Johnson, T.R. Cummins, D.M. Bers, and A. Hudmon. 2012. Ca^{2+}/calmodulin-dependent protein kinase II (CaMKII) regulates cardiac sodium channel NaV1.5 gating by multiple phosphorylation sites. *J. Biol. Chem.* 287:19856–19869. https://doi.org/10.1074/jbc.M111.322537

Boehmer, C., V. Wilhelm, M. Palmada, S. Wallisch, G. Henke, H. Brinkmeier, P. Cohen, B. Pieske, and F. Lang. 2003. Serum and glucocorticoid inducible kinases in the regulation of the cardiac sodium channel SCN5A. *Cardiovasc. Res.* 57:1079–1084. https://doi.org/10.1016/S0008-6363(02)00837-4

Burel, S., F.C. Coyan, M. Lorenzini, M.R. Meyer, C.F. Lichti, J.H. Brown, G. Loussouarn, F. Charpentier, J.M. Nerbonne, R.R. Townsend, et al. 2017. C-terminal phosphorylation of $Na_V1.5$ impairs FGF13-dependent regulation of channel inactivation. *J. Biol. Chem.* 292:17431–17448. https://doi.org/10.1074/jbc.M117.787788

Chen, Z.W., K. Fuchs, W. Sieghart, R.R. Townsend, and A.S. Evers. 2012. Deep amino acid sequencing of native brain $GABA_A$ receptors using high-resolution mass spectrometry. *Mol. Cell. Proteomics.* 11:M111.011445. https://doi.org/10.1074/mcp.M111.011445

Das, R.K., and R.V. Pappu. 2013. Conformations of intrinsically disordered proteins are influenced by linear sequence distributions of oppositely charged residues. *Proc. Natl. Acad. Sci. USA.* 110:13392–13397. https://doi.org/10.1073/pnas.1304749110

Dybkova, N., S. Ahmad, S. Pabel, P. Tirilomis, N. Hartmann, T.H. Fischer, P. Bengel, T. Tirilomis, S. Ljubojevic, A. Renner, et al. 2018. Differential regulation of sodium channels as a novel proarrhythmic mechanism in the human failing heart. *Cardiovasc. Res.* 114:1728–1737. https://doi.org/10.1093/cvr/cvy152

Erde, J., R.R. Loo, and J.A. Loo. 2014. Enhanced FASP (eFASP) to increase proteome coverage and sample recovery for quantitative proteomic experiments. *J. Proteome Res.* 13:1885–1895. https://doi.org/10.1021/pr4010019

Gao, S., D. Ho, D.E. Vatner, and S.F. Vatner. 2011. Echocardiography in Mice. *Curr. Protoc. Mouse Biol.* 1:71–83.

Glynn, P., H. Musa, X. Wu, S.D. Unudurthi, S. Little, L. Qian, P.J. Wright, P.B. Radwanski, S. Gyorke, P.J. Mohler, and T.J. Hund. 2015. Voltage-gated sodium channel phosphorylation at Ser571 regulates late current, arrhythmia, and cardiac function in vivo. *Circulation.* 132:567–577. https://doi.org/10.1161/CIRCULATIONAHA.114.015218

Herren, A.W., D.M. Weber, R.R. Rigor, K.B. Margulies, B.S. Phinney, and D.M. Bers. 2015. CaMKII phosphorylation of Na(V)1.5: novel in vitro sites identified by mass spectrometry and reduced S516 phosphorylation in human heart failure. *J. Proteome Res.* 14:2298–2311. https://doi.org/10.1021/acs.jproteome.5b00107

Holehouse, A.S., and R.V. Pappu. 2018. Collapse transitions of proteins and the interplay among backbone, sidechain, and solvent interactions. *Annu. Rev. Biophys.* 47:19–39. https://doi.org/10.1146/annurev-biophys-070317-032838

Hund, T.J., O.M. Koval, J. Li, P.J. Wright, L. Qian, J.S. Snyder, H. Gudmundsson, C.F. Kline, N.P. Davidson, N. Cardona, et al. 2010. A β(IV)-spectrin/CaMKII signaling complex is essential for membrane excitability in mice. *J. Clin. Invest.* 120:3508–3519. https://doi.org/10.1172/JCI43621

Hunter, T. 2012. Why nature chose phosphate to modify proteins. *Philos. Trans. R. Soc. Lond. B Biol. Sci.* 367:2513–2516. https://doi.org/10.1098/rstb.2012.0013

Iakoucheva, L.M., P. Radivojac, C.J. Brown, T.R. O'Connor, J.G. Sikes, Z. Obradovic, and A.K. Dunker. 2004. The importance of intrinsic disorder

for protein phosphorylation. *Nucleic Acids Res.* 32:1037–1049. https://doi.org/10.1093/nar/gkh253

Iqbal, S.M., M. Aufy, W. Shabbir, and R. Lemmens-Gruber. 2018. Identification of phosphorylation sites and binding pockets for modulation of Na_V 1.5 channel by Fyn tyrosine kinase. *FEBS J.* 285:2520–2530. https://doi.org/10.1111/febs.14496

Johnson, H., and F.M. White. 2012. Toward quantitative phosphotyrosine profiling in vivo. *Semin. Cell Dev. Biol.* 23:854–862. https://doi.org/10.1016/j.semcdb.2012.05.008

Juang, J.-M.J., C.-T. Tsai, L.-Y. Lin, Y.-B. Liu, C.-C. Yu, J.-J. Hwang, J.-J. Chen, F.-C. Chiu, W.-J. Chen, C.-D. Tseng, et al. 2015. Unique clinical characteristics and SCN5A mutations in patients with Brugada syndrome in Taiwan. *J. Formos. Med. Assoc.* 114:620–626. https://doi.org/10.1016/j.jfma.2013.02.002

Kääb, S., J. Dixon, J. Duc, D. Ashen, M. Näbauer, D.J. Beuckelmann, G. Steinbeck, D. McKinnon, and G.F. Tomaselli. 1998. Molecular basis of transient outward potassium current downregulation in human heart failure: a decrease in Kv4.3 mRNA correlates with a reduction in current density. *Circulation.* 98:1383–1393. https://doi.org/10.1161/01.CIR.98.14.1383

Kapplinger, J.D., D.J. Tester, B.A. Salisbury, J.L. Carr, C. Harris-Kerr, G.D. Pollevick, A.A.M. Wilde, and M.J. Ackerman. 2009. Spectrum and prevalence of mutations from the first 2,500 consecutive unrelated patients referred for the FAMILION long QT syndrome genetic test. *Heart Rhythm.* 6:1297–1303. https://doi.org/10.1016/j.hrthm.2009.05.021

Koval, O.M., J.S. Snyder, R.M. Wolf, R.E. Pavlovicz, P. Glynn, J. Curran, N.D. Leymaster, W. Dun, P.J. Wright, N. Cardona, et al. 2012. Ca^{2+}/calmodulin-dependent protein kinase II-based regulation of voltage-gated Na^+ channel in cardiac disease. *Circulation.* 126:2084–2094. https://doi.org/10.1161/CIRCULATIONAHA.112.105320

Liu, M., L. Gu, M.S. Sulkin, H. Liu, E.M. Jeong, I. Greener, A. Xie, I.R. Efimov, and S.C. Dudley Jr. 2013. Mitochondrial dysfunction causing cardiac sodium channel downregulation in cardiomyopathy. *J. Mol. Cell. Cardiol.* 54:25–34. https://doi.org/10.1016/j.yjmcc.2012.10.011

Liu, X., Z. Chen, Z. Han, Y. Liu, X. Wu, Y. Peng, W. Di, R. Lan, B. Sun, B. Xu, and W. Xu. 2019. AMPK-mediated degradation of Nav1.5 through autophagy. *FASEB J.* 33:5366–5376. https://doi.org/10.1096/fj.201801583RR

Luo, L., F. Ning, Y. Du, B. Song, D. Yang, S.C. Salvage, Y. Wang, J.A. Fraser, S. Zhang, A. Ma, and T. Wang. 2017. Calcium-dependent Nedd4-2 upregulation mediates degradation of the cardiac sodium channel Nav1.5: implications for heart failure. *Acta Physiol. (Oxf.).* 221:44–58. https://doi.org/10.1111/apha.12872

Makielski, J.C., B. Ye, C.R. Valdivia, M.D. Pagel, J. Pu, D.J. Tester, and M.J. Ackerman. 2003. A ubiquitous splice variant and a common polymorphism affect heterologous expression of recombinant human SCN5A heart sodium channels. *Circ. Res.* 93:821–828. https://doi.org/10.1161/01.RES.0000096652.14509.96

Maltsev, V.A., N. Silverman, H.N. Sabbah, and A.I. Undrovinas. 2007. Chronic heart failure slows late sodium current in human and canine ventricular myocytes: implications for repolarization variability. *Eur. J. Heart Fail.* 9:219–227. https://doi.org/10.1016/j.ejheart.2006.08.007

Maltsev, V.A., V. Reznikov, N.A. Undrovinas, H.N. Sabbah, and A. Undrovinas. 2008. Modulation of late sodium current by Ca^{2+}, calmodulin, and CaMKII in normal and failing dog cardiomyocytes: similarities and differences. *Am. J. Physiol. Heart Circ. Physiol.* 294:H1597–H1608. https://doi.org/10.1152/ajpheart.00484.2007

Mao, A.H., S.L. Crick, A. Vitalis, C.L. Chicoine, and R.V. Pappu. 2010. Net charge per residue modulates conformational ensembles of intrinsically disordered proteins. *Proc. Natl. Acad. Sci. USA.* 107:8183–8188. https://doi.org/10.1073/pnas.0911107107

Marionneau, C., and H. Abriel. 2015. Regulation of the cardiac Na^+ channel NaV1.5 by post-translational modifications. *J. Mol. Cell. Cardiol.* 82:36–47. https://doi.org/10.1016/j.yjmcc.2015.02.013

Marionneau, C., Y. Carrasquillo, A.J. Norris, R.R. Townsend, L.L. Isom, A.J. Link, and J.M. Nerbonne. 2012a. The sodium channel accessory subunit Navβ1 regulates neuronal excitability through modulation of repolarizing voltage-gated K^+ channels. *J. Neurosci.* 32:5716–5727. https://doi.org/10.1523/JNEUROSCI.6450-11.2012

Marionneau, C., C.F. Lichti, P. Lindenbaum, F. Charpentier, J.M. Nerbonne, R.R. Townsend, and J. Mérot. 2012b. Mass spectrometry-based identification of native cardiac Nav1.5 channel α subunit phosphorylation sites. *J. Proteome Res.* 11:5994–6007. https://doi.org/10.1021/pr300702c

Martin, E.W., A.S. Holehouse, C.R. Grace, A. Hughes, R.V. Pappu, and T. Mittag. 2016. Sequence determinants of the conformational properties of an intrinsically disordered protein prior to and upon multisite phosphorylation. *J. Am. Chem. Soc.* 138:15323–15335. https://doi.org/10.1021/jacs.6b10272

Mishra, S., V. Reznikov, V.A. Maltsev, N.A. Undrovinas, H.N. Sabbah, and A. Undrovinas. 2015. Contribution of sodium channel neuronal isoform Nav1.1 to late sodium current in ventricular myocytes from failing hearts. *J. Physiol.* 593:1409–1427. https://doi.org/10.1113/jphysiol.2014.278259

Noyes, A.M., A. Zhou, G. Gao, L. Gu, S. Day, J. Andrew Wasserstrom, and S.C. Dudley. 2017. Abnormal sodium channel mRNA splicing in hypertrophic cardiomyopathy. *Int. J. Cardiol.* 249:282–286. https://doi.org/10.1016/j.ijcard.2017.08.071

Pei, Z., Y. Xiao, J. Meng, A. Hudmon, and T.R. Cummins. 2016. Cardiac sodium channel palmitoylation regulates channel availability and myocyte excitability with implications for arrhythmia generation. *Nat. Commun.* 7:12035. https://doi.org/10.1038/ncomms12035

Plant, L.D., D. Xiong, J. Romero, H. Dai, and S.A.N. Goldstein. 2020. Hypoxia produces pro-arrhythmic late sodium current in cardiac myocytes by SUMOylation of Na_V1.5 channels. *Cell Rep.* 30:2225–2236.e4. https://doi.org/10.1016/j.celrep.2020.01.025

Remme, C.A., A.A.M. Wilde, and C.R. Bezzina. 2008. Cardiac sodium channel overlap syndromes: different faces of SCN5A mutations. *Trends Cardiovasc. Med.* 18:78–87. https://doi.org/10.1016/j.tcm.2008.01.002

Remme, C.A., and C.R. Bezzina. 2010. Sodium channel (dys)function and cardiac arrhythmias. *Cardiovasc. Ther.* 28:287–294. https://doi.org/10.1111/j.1755-5922.2010.00210.x

Rivaud, M.R., E. Agullo-Pascual, X. Lin, A. Leo-Macias, M. Zhang, E. Rothenberg, C.R. Bezzina, M. Delmar, and C.A. Remme. 2017. Sodium channel remodeling in subcellular microdomains of murine failing cardiomyocytes. *J. Am. Heart Assoc.* 6:e007622. https://doi.org/10.1161/JAHA.117.007622

Schneider, C., R.A. Newman, D.R. Sutherland, U. Asser, and M.F. Greaves. 1982. A one-step purification of membrane proteins using a high efficiency immunomatrix. *J. Biol. Chem.* 257:10766–10769.

Schubert, B., A.M. VanDongen, G.E. Kirsch, and A.M. Brown. 1989. Beta-adrenergic inhibition of cardiac sodium channels by dual G-protein pathways. *Science.* 245:516–519. https://doi.org/10.1126/science.2547248

Shang, L.L., A.E. Pfahnl, S. Sanyal, Z. Jiao, J. Allen, K. Banach, J. Fahrenbach, D. Weiss, W.R. Taylor, A.M. Zafari, and S.C. Dudley Jr. 2007. Human heart failure is associated with abnormal C-terminal splicing variants in the cardiac sodium channel. *Circ. Res.* 101:1146–1154. https://doi.org/10.1161/CIRCRESAHA.107.152918

Toischer, K., N. Hartmann, S. Wagner, T.H. Fischer, J. Herting, B.C. Danner, C.M. Sag, T.J. Hund, P.J. Mohler, L. Belardinelli, et al. 2013. Role of late sodium current as a potential arrhythmogenic mechanism in the progression of pressure-induced heart disease. *J. Mol. Cell. Cardiol.* 61:111–122. https://doi.org/10.1016/j.yjmcc.2013.03.021

Valdivia, C.R., W.W. Chu, J. Pu, J.D. Foell, R.A. Haworth, M.R. Wolff, T.J. Kamp, and J.C. Makielski. 2005. Increased late sodium current in myocytes from a canine heart failure model and from failing human heart. *J. Mol. Cell. Cardiol.* 38:475–483. https://doi.org/10.1016/j.yjmcc.2004.12.012

Varga, Z., W. Zhu, A.R. Schubert, J.L. Pardieck, A. Krumholz, E.J. Hsu, M.A. Zaydman, J. Cui, and J.R. Silva. 2015. Direct measurement of cardiac Na^+ channel conformations reveals molecular pathologies of inherited mutations. *Circ. Arrhythm. Electrophysiol.* 8:1228–1239. https://doi.org/10.1161/CIRCEP.115.003155

Vassilev, P.M., T. Scheuer, and W.A. Catterall. 1988. Identification of an intracellular peptide segment involved in sodium channel inactivation. *Science.* 241:1658–1661. https://doi.org/10.1126/science.2458625

Vitalis, A., and R.V. Pappu. 2009a. ABSINTH: a new continuum solvation model for simulations of polypeptides in aqueous solutions. *J. Comput. Chem.* 30:673–699. https://doi.org/10.1002/jcc.21005

Vitalis, A., and R.V. Pappu. 2009b. Methods for Monte Carlo simulations of biomacromolecules. *Annu. Rep. Comput. Chem.* 5:49–76. https://doi.org/10.1016/S1574-1400(09)00503-9

Wagner, S., N. Dybkova, E.C. Rasenack, C. Jacobshagen, L. Fabritz, P. Kirchhof, S.K. Maier, T. Zhang, G. Hasenfuss, J.H. Brown, et al. 2006. Ca^{2+}/calmodulin-dependent protein kinase II regulates cardiac Na^+ channels. *J. Clin. Invest.* 116:3127–3138. https://doi.org/10.1172/JCI26620

Wiśniewski, J.R., A. Zougman, N. Nagaraj, and M. Mann. 2009. Universal sample preparation method for proteome analysis. *Nat. Methods.* 6:359–362. https://doi.org/10.1038/nmeth.1322

Wright, P.E., and H.J. Dyson. 2015. Intrinsically disordered proteins in cellular signalling and regulation. *Nat. Rev. Mol. Cell Biol.* 16:18–29. https://doi.org/10.1038/nrm3920

Xi, Y., G. Wu, L. Yang, K. Han, Y. Du, T. Wang, X. Lei, X. Bai, and A. Ma. 2009. Increased late sodium currents are related to transcription of neuronal isoforms in a pressure-overload model. *Eur. J. Heart Fail.* 11:749–757. https://doi.org/10.1093/eurjhf/hfp092

Yu, P., L. Hu, J. Xie, S. Chen, L. Huang, Z. Xu, X. Liu, Q. Zhou, P. Yuan, X. Yan, et al. 2018. O-GlcNAcylation of cardiac Nav1.5 contributes to the development of arrhythmias in diabetic hearts. *Int. J. Cardiol.* 260:74–81. https://doi.org/10.1016/j.ijcard.2018.02.099

Zhang, J., L. Xin, B. Shan, W. Chen, M. Xie, D. Yuen, W. Zhang, Z. Zhang, G.A. Lajoie, and B. Ma. 2012. PEAKS DB: de novo sequencing assisted database search for sensitive and accurate peptide identification. *Mol. Cell. Proteomics.* 11:M111.010587. https://doi.org/10.1074/mcp.M111.010587

Zicha, S., V.A. Maltsev, S. Nattel, H.N. Sabbah, and A.I. Undrovinas. 2004. Post-transcriptional alterations in the expression of cardiac Na^+ channel subunits in chronic heart failure. *J. Mol. Cell. Cardiol.* 37:91–100. https://doi.org/10.1016/j.yjmcc.2004.04.003

Zimmer, T., and R. Surber. 2008. SCN5A channelopathies--an update on mutations and mechanisms. *Prog. Biophys. Mol. Biol.* 98:120–136. https://doi.org/10.1016/j.pbiomolbio.2008.10.005

Supplemental material

A

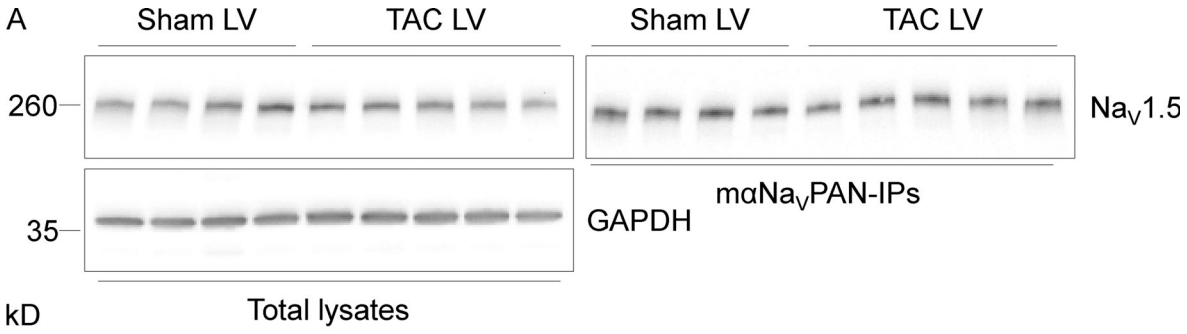

B

Sample	Channel	Normalization factor
Sham LV 1	TMT10-127N	1.04
Sham LV 2	TMT10-127C	0.99
Sham LV 3	TMT10-128N	1.15
Sham LV 4	TMT10-128C	0.99
TAC LV 1	TMT10-129N	1.17
TAC LV 2	TMT10-129C	1.00
TAC LV 3	TMT10-130N	1.26
TAC LV 4	TMT10-130C	1.08
TAC LV 5	TMT10-131	1.22

C

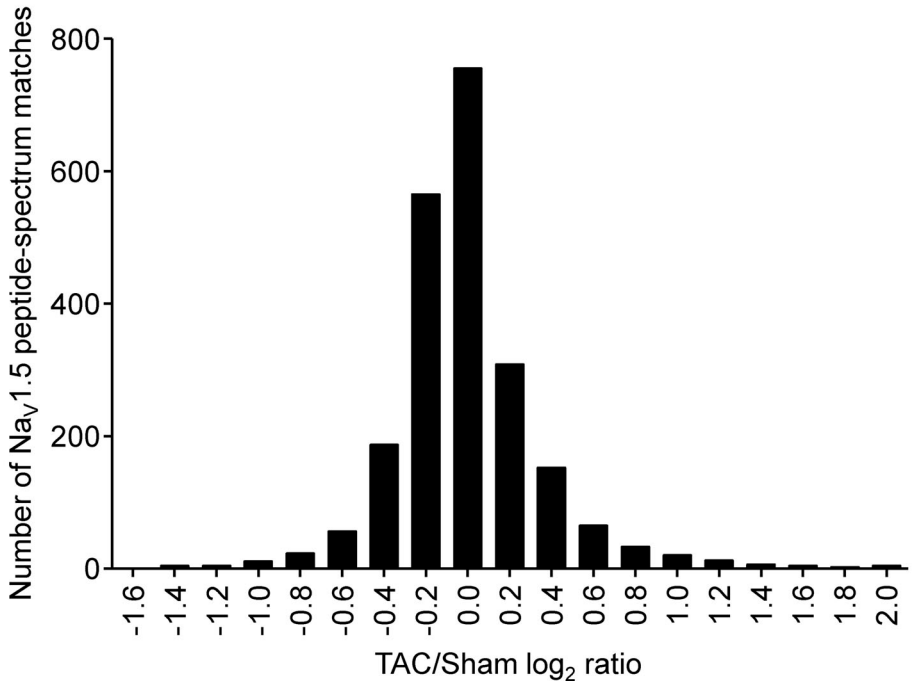

Figure S1. **IP yields and relative quantification of $Na_V1.5$ peptide abundances from sham and TAC mouse left ventricles (LVs). (A)** Representative Western blots of total lysates and mαNa_VPAN-IPs from sham and TAC LVs probed with the anti-$Na_V1.5$ rabbit polyclonal (Rbα$Na_V1.5$) and anti-GAPDH mouse mAbs. **(B)** Normalization factors used in MS1 and MS2 analyses to correct for technical variabilities in $Na_V1.5$ protein abundance in mαNa_VPAN-IPs from sham and TAC LVs. **(C)** Distribution of TAC/sham log_2-normalized ratios of $Na_V1.5$ peptide spectrum matches. Both biochemical (A) and MS (B and C) analyses of $Na_V1.5$ IP yields and peptide relative abundance demonstrate low technical variability.

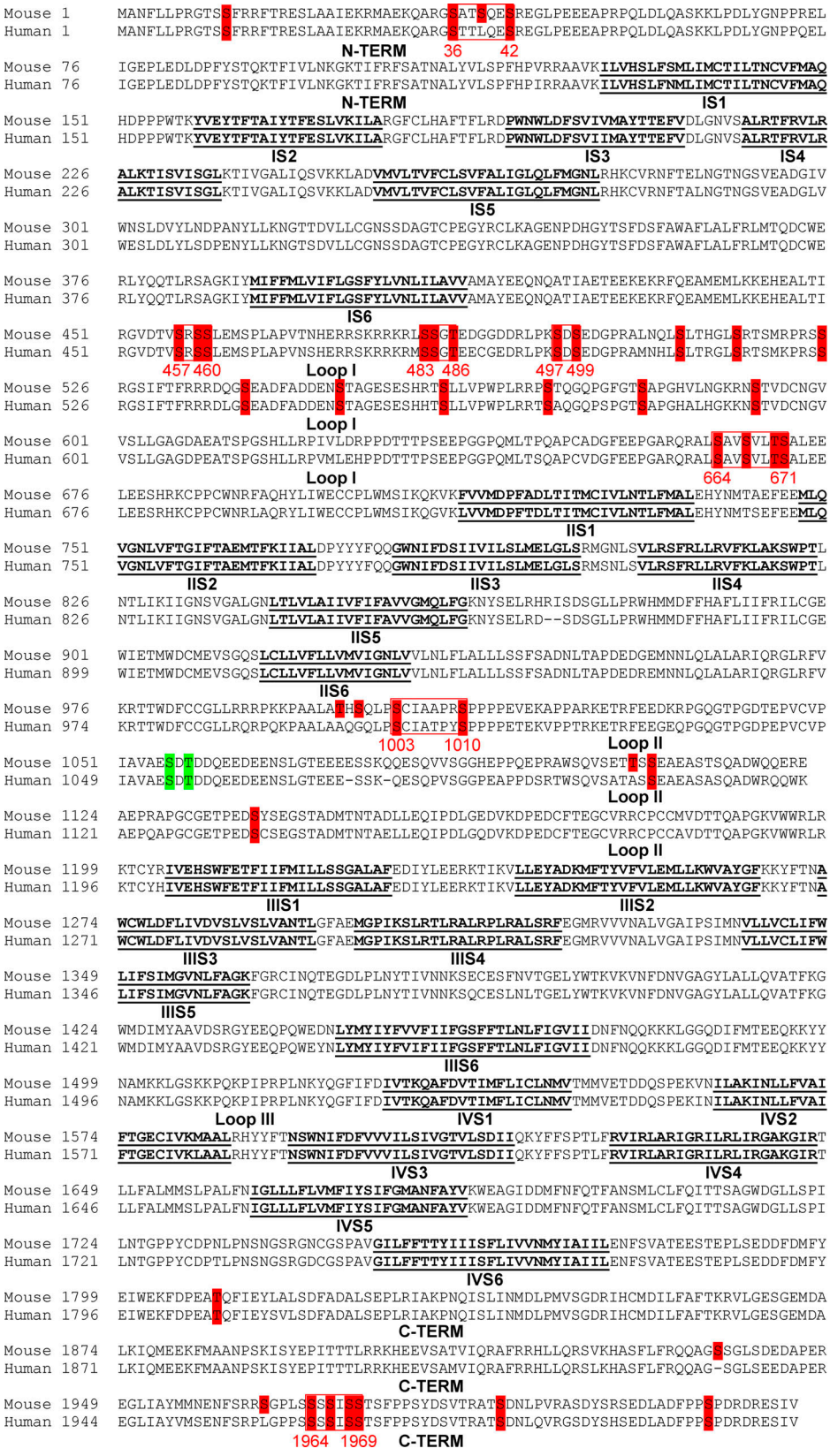

Figure S2. **Conservation of phosphorylation sites in mouse and human $Na_V1.5$.** The mouse (reference sequence NP_001240789.1) and human (NP_000326.2) $Na_V1.5$ sequences are aligned, and phosphorylation sites identified on the mouse sequence and conserved in human are highlighted in red. Two phosphorylation site locations are possible at amino acids S1056-T1058 (in green). Transmembrane segments (S1-S6) in each domain (I–IV) are in bold and underlined in black; loops I, II, and III correspond to interdomains I–II, II–III, and III–IV, respectively. The seven phosphorylation clusters analyzed electrophysiologically are boxed in red. C-TERM, C terminus; N-TERM, N terminus.

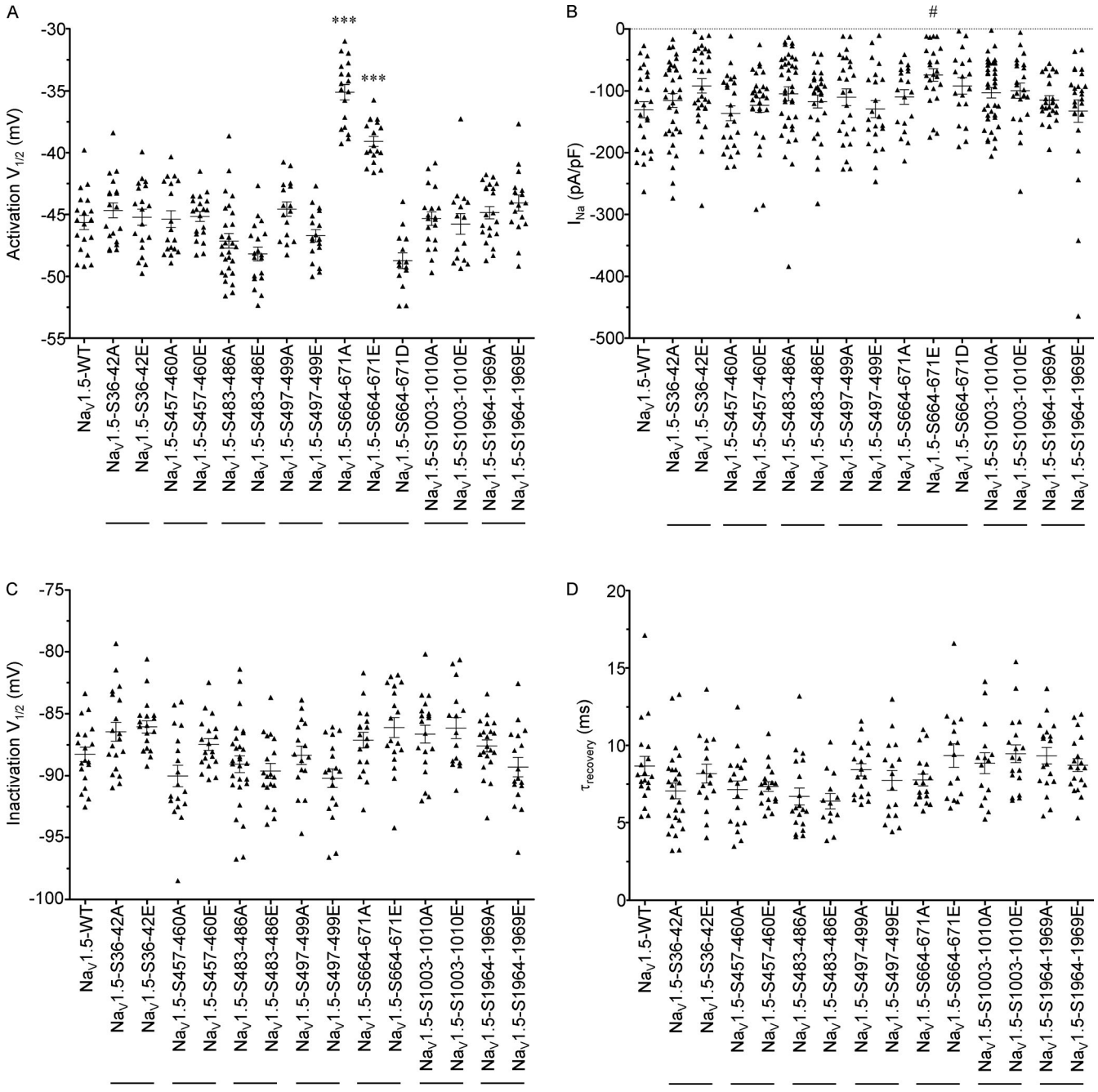

Figure S3. **Distributions and mean ± SEM membrane potentials for half-activation and half-inactivation, peak I_{Na} densities, and time constants of recovery from inactivation of WT and mutant $Na_V1.5$ channels.** Half-activation (A), peak I_{Na} densities (B), half-inactivation (C), and time constants of recovery from inactivation (D) of WT and mutant $Na_V1.5$ channels. Currents were recorded as described in the legend to Fig. 3. The I_{Na} densities presented were determined from analyses of records obtained on depolarizations to −20 mV (HP = −120 mV). #, $P < 0.05$ versus $Na_V1.5$-WT, one-way ANOVA followed by the Dunnett's post-hoc test. ***, $P < 0.001$ versus $Na_V1.5$-WT, Kruskal-Wallis followed by the Dunn's post-hoc test. Current densities, time- and voltage-dependent properties, and statistical comparisons across groups are provided in Table 3.

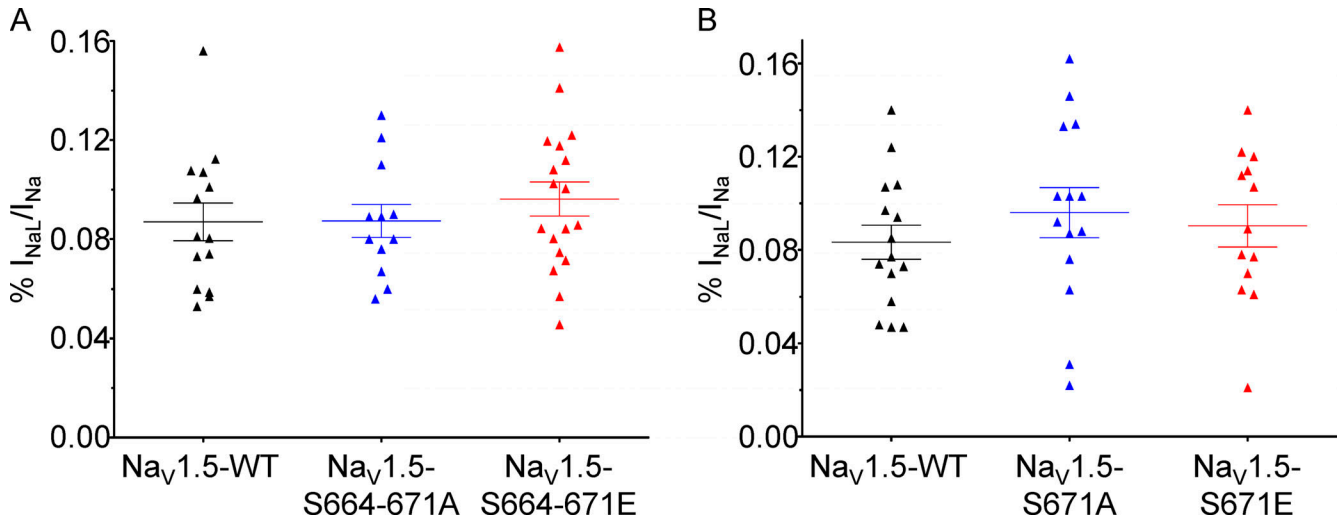

Figure S4. **Distributions and mean ± SEM. (A and B)** TTX-sensitive I_{NaL} densities of quadruple S664-671 (A) and simple S671 (B) $Na_V1.5$ phosphomutants. TTX-sensitive I_{NaL} were evoked during prolonged depolarizations (350 ms at −20 mV; HP = −120 mV) 48 h after transfection of HEK-293 cells with WT (black), phosphosilent (blue), and phosphomimetic (red) $Na_V1.5$ channels and $Na_V\beta1$. No significant differences between mutant and WT channels were observed.

Provided online are three tables and one data file. Table S1 lists echocardiographic parameters of sham and TAC mice before and 5 wk after surgery. Table S2 summarizes $Na_V1.5$ phosphorylation sites identified in the present and previous studies. Table S3 lists phosphorylation sites, phosphopeptides, and site-discriminating ions identified in coimmunoprecipitated NaVα subunits from sham and TAC mouse left ventricles using MS. Data S1 lists representative MS/MS spectra of singly or doubly phosphorylated NaV1.5, NaV1.4, and NaV1.3 tryptic peptides.